Miocene climate change recorded in the chemical and isotopic (Pb, Nd, Hf) signature of Southern Ocean sediments.

Ivan Vlastélic, M. Carpentier, Eric Lewin

Miocene climate change recorded in the chemical and isotopic (Pb, Nd, Hf) signature of Southern Ocean sediments

Ivan Vlastélic, Marion Carpentier, and Éric Lewin

Laboratoire de Géodynamique des Chaînes Alpines, 1381 Rue de la Piscine, BP 53, 38041 Grenoble Cedex 9, France (ivan.vlastelic@ujf-grenoble.fr)

[1] The Middle Miocene transition from carbonate to biosilica sedimentation at DSDP site 266 (Australian-Antarctic basin) reflects a global transition toward a colder climate. The $^{143}Nd/^{144}Nd$, $^{176}Hf/^{177}Hf$, and Al/Ti of bulk sediments display systematic, coupled variations through time, which have been attributed to a change of the detrital source. This change could correspond to a reduction of input from the Antarctic continent, an increase of input from the Kerguelen volcanic province, or both. Mixing models based on Nd isotopes and Al/Ti suggest a 30–40% reduction of Antarctic input and an equivalent increase of Kerguelen input during the Miocene. Reduction of Antarctic input may result from the formation of a stable East Antarctic ice sheet. Consistently, Pb isotopes and trace element systematics suggest a change of weathering style during the Miocene, with an increase in physical weathering, or a reduction of chemical weathering, after 15 Ma. Increase of Kerguelen input may reflect the initiation, or enhancement, of the Antarctic Circumpolar Current (ACC), thus raising the possibility of a simultaneous onset of North Atlantic Deep Water production and the ACC during the Middle Miocene. In addition, large geochemical oscillations occurred during the Pliocene, possibly reflecting fluctuation in strength of the ACC or, alternatively, periods of instability of the Antarctic ice sheet.

1. Introduction

[2] A major step in the Tertiary transition toward cold polar climate occurred in the middle Miocene [*Zachos et al.*, 2001]. The prevalent view suggests global cooling and development of polar ice sheets as the Antarctic Circumpolar Current (ACC) progressively connected the three main oceanic basins and thermally isolated the Antarctic continent [*Shackleton and Kennett*, 1975; *Kennett*, 1977; *Miller et al.*, 1987; *Exon et al.*, 2002]. A change in the geographic distribution of carbonate and biosilica sediments near the middle Miocene may also reflect a major evolution of the global oceanic circulation toward the present-day thermo-haline circulation driven by high-latitude deepwater production [*Woodruff and Savin*, 1989]. High-resolution oxygen isotope records reveal that a period of climatic optimum from 17 to 15 Ma (Middle Miocene Climatic Optimum, or MMCO) was followed by a sequence of cooling events from 15 to 12.5 Ma (Middle Miocene Shift, or MMS), which have been related to a major growth of the East Antarctic ice sheet [*Flower and Kennett*, 1995]. Although there is a general consensus regarding these main features, the connection between the main hydrographic and cryospheric events, as well as the role played by

the different water masses, is still subject to debate. For instance, some authors have suggested that Antarctic glaciation predates the middle Miocene [*Matthews and Poore*, 1980; *Miller et al.*, 1991; *Ehrmann and Mackensen*, 1992]. There is also some disagreement regarding the early Miocene deepwater circulation pattern and the role played by plate tectonics in hydrographic changes (see *Wright et al.* [1992] for a synthesis).

[3] The Miocene global change has been essentially studied using stable isotopes (O and C), fossil assemblages and sedimentation patterns. The aim of this paper is to use the geochemical data and radiogenic isotope systematics of abyssal sediments to provide a complementary view on the processes occurring during that period. The signature of long-lived radiogenic isotopes (Nd, Hf, Pb) in marine sediments first reflects the composition of the source regions eroded and the subsequent distribution by oceanic circulation. In addition, sedimentary processes such as grain size-dependent transportation, mineralogical sorting and interaction with seawater influence in a complex manner the isotopic signatures of deep-sea sediments. Taking these processes into account, radiogenic isotopes can be used to constrain the rate of continental weathering as well as paleo-currents or paleo-climates. Analyses of separated size-fractions or separated phases (authigenic or detrital) have been used to distinguish the different signals contained in sediments [*Rutberg et al.*, 2000; *Bayon et al.*, 2002; *Piotrowski et al.*, 2004]. However, when the elements of interest are principally concentrated in the terrigenous fraction, the message delivered by bulk sediment analysis may be sufficiently clear to infer change of detrital sources [*Abouchami and Zabel*, 2003; this study].

[4] The Circum-Antarctic Ocean is a suitable place for such study because of its key role in controlling global climate and its expected sensitivity to glaciation on the Antarctic continent. The Circum-Antarctic distribution of dissolved Nd and Pb isotopes inferred from the surfaces of Fe-Mn deposits shows a clear provinciality, suggesting that dominant hydrographic processes have persisted over the last 10^6 years [*Abouchami and Goldstein*, 1995; *Albarède et al.*, 1997]. On the other hand, studies of high-resolution sediment cores have revealed systematic changes of elemental provenance in the Southern Ocean that are clearly linked to quaternary glacial-interglacial cycles [*Bareille et al.*, 1994; *Rutberg et al.*, 2000; *Walter et al.*, 2000; *Bayon et al.*, 2003]. For

example, Nd isotopes have been used to suggest a reduced flux of North Atlantic Deep Water (NADW) to the Southern Ocean during glacial periods [*Rutberg et al.*, 2000]. The middle Miocene climate change and related processes could have influenced sediment provenance in the Southern Ocean as well.

[5] Inspection of the literature reveals that few long-term seawater Nd, Hf and Pb isotopic record have been reported for the Southern Ocean. A ferromanganese crust located at 28°S in the south Indian Ocean (crust 109D-C) showed tiny isotopic variations over the last 20 Ma [*O'Nions et al.*, 1998; *Piotrowski et al.*, 2000] suggesting long-term stability of the ACC. More recently, five additional records (from 3 to 10 Ma) on high southern latitude Fe-Mn deposits have been used to infer a "continuous and strong export of NADW" to the Southern Ocean from 14 to 3 Ma and a progressive reduction of that export since the onset of Northern Hemisphere glaciation [*Frank et al.*, 2002]. On the other hand, the provenance of terrigenous sediments deposited in the southern Indian basin (59°36′S) has varied since the late Miocene, possibly reflecting change of Antarctic climate and derived ice sheet stability [*Joseph et al.*, 2002]. The absence of a radiogenic isotope record covering the entire Miocene at high latitudes in the Southern Ocean was one of the motivations of this study.

2. Site Selection and Core Description

[6] Site selection took into account two observations: (1) The magnitude of the middle Miocene oxygen isotopic shift is the greatest at higher southern latitudes and at greater depths [*Woodruff and Savin*, 1991]. (2) The pre-anthropogenic distribution of Pb isotopes inferred from Fe-Mn deposits shows a clear provinciality within the Circum-Antarctic Ocean (Figure 1a) [*Abouchami and Goldstein*, 1995], the most radiogenic values (indicative of continental origin) being confined to great depths in the Australian-Antarctic basin [*Vlastélic et al.*, 2001] (Figure 1b). Site 266 of DSDP leg 28 (56°24.13′S, 110°06.70′E) is located at great depth (4200 m) in the Australian Antarctic Basin and thus is ideally suited for the purpose of this study. In addition, site 266 provides a continuous sedimentary sequence for the past 23 Ma. The diversity of microfossil groups allows a reliable and relatively precise (±1 Ma) stratigraphy to be established, which was reinforced by a good agreement between the age of basal sediments and that of the basaltic crust inferred from magnetic
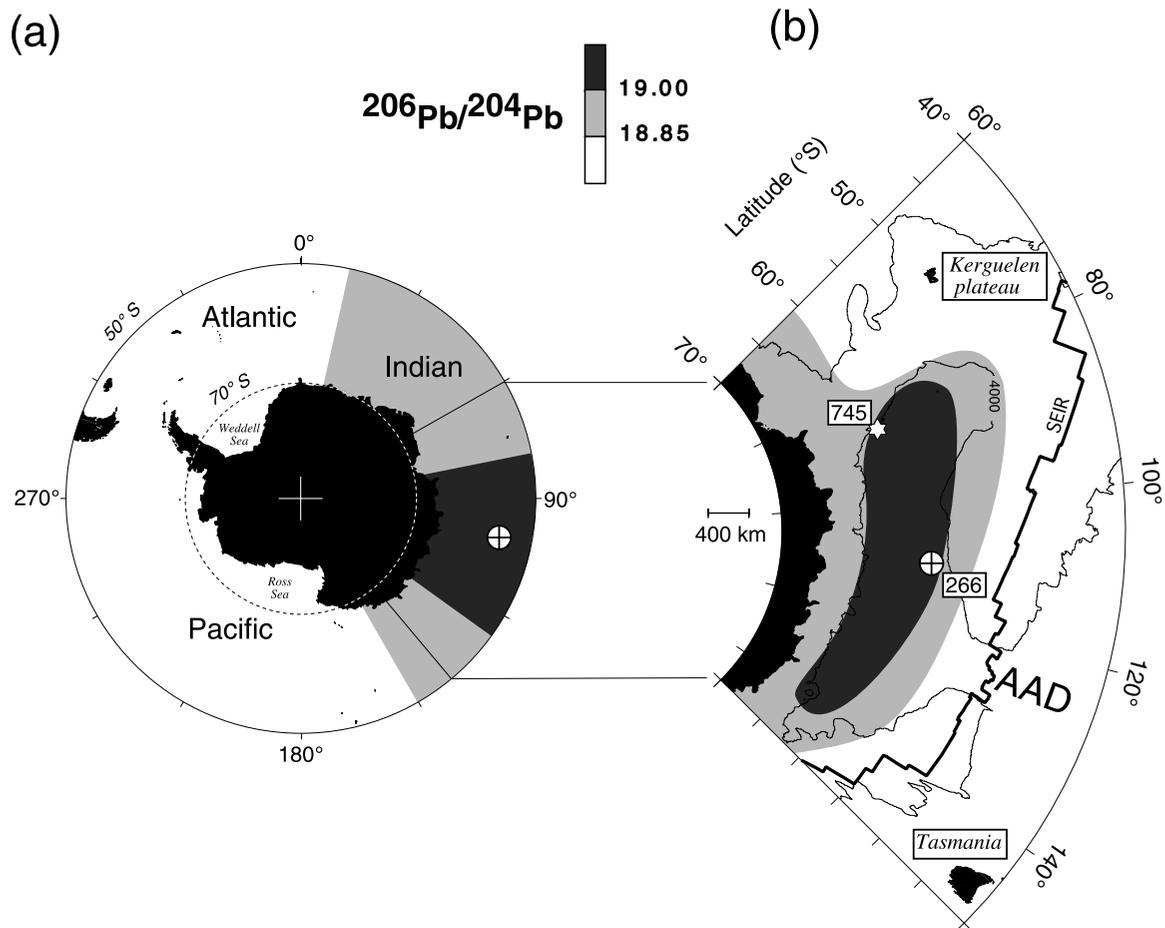
Figure 1. Maps of Southern Ocean showing the location of DSDP site 266 (this study) and the nearby ODP site 745. The isotopic composition of natural lead in seawater, as inferred from Fe-Mn deposits [*Abouchami and Goldstein*, 1995; *Vlastélic et al.*, 2001], is indicated.

anomaly lineations (Figure 2a) [*Hayes et al.*, 1975]. The sedimentation rate ranges from 5 to 40 m/Ma and periods with high accumulation rates (0–4 Ma, 14–16 Ma) can be distinguished from periods of slow deposition (5–14 Ma) (Figure 2b). A transition from dominantly carbonaceous to dominantly biosiliceous sediments occurred at about 15 Ma (Figure 2c). Although such a transition could theoretically reflect the subsidence of the sedimentary pile as it migrated away from the Southeast Indian Ridge, the appearance of ice-rafted debris at that time [*Hayes et al.*, 1975], the correspondence with the oxygen isotopic shift (Figure 2d), and the global occurrence of such a transition at that time (the "silica switch" [*Keller and Barron*, 1983; *Woodruff and Savin*, 1989]) all suggest that site 266 lithology has recorded the middle Miocene climate change. In detail, the core can be divided into three units. The uppermost unit (0–6 Ma) is made up of diatomaceous ooze with minor amounts of carbonate and clay; the transitional

unit (6–15 Ma) consists of a mixed sequence of diatom and nanno oozes, and diatom- and nanno-rich clays; the lower unit (15–23 Ma) is dominantly nanno chalks with minor nanno claystones. The biogenic component (nanno-fossils + diatoms) is predominant in units I and III, while the clay fraction is the most abundant in unit II (Figure 2c).

3. Samples and Methods

[7] Twenty-two samples regularly spaced along the core were obtained from the ODP repository of the Lamont-Doherty Earth Observatory. Samples were dried for 12 hours at 500°C. Because separation of phases from sediments can be neither rigorously quantitative nor reproducible (in particular like sediments from site 266, whose lithology varies widely), no attempt was made to separate sediment fractions. Instead, our approach consisted of a complete dissolution of the bulk sediment followed
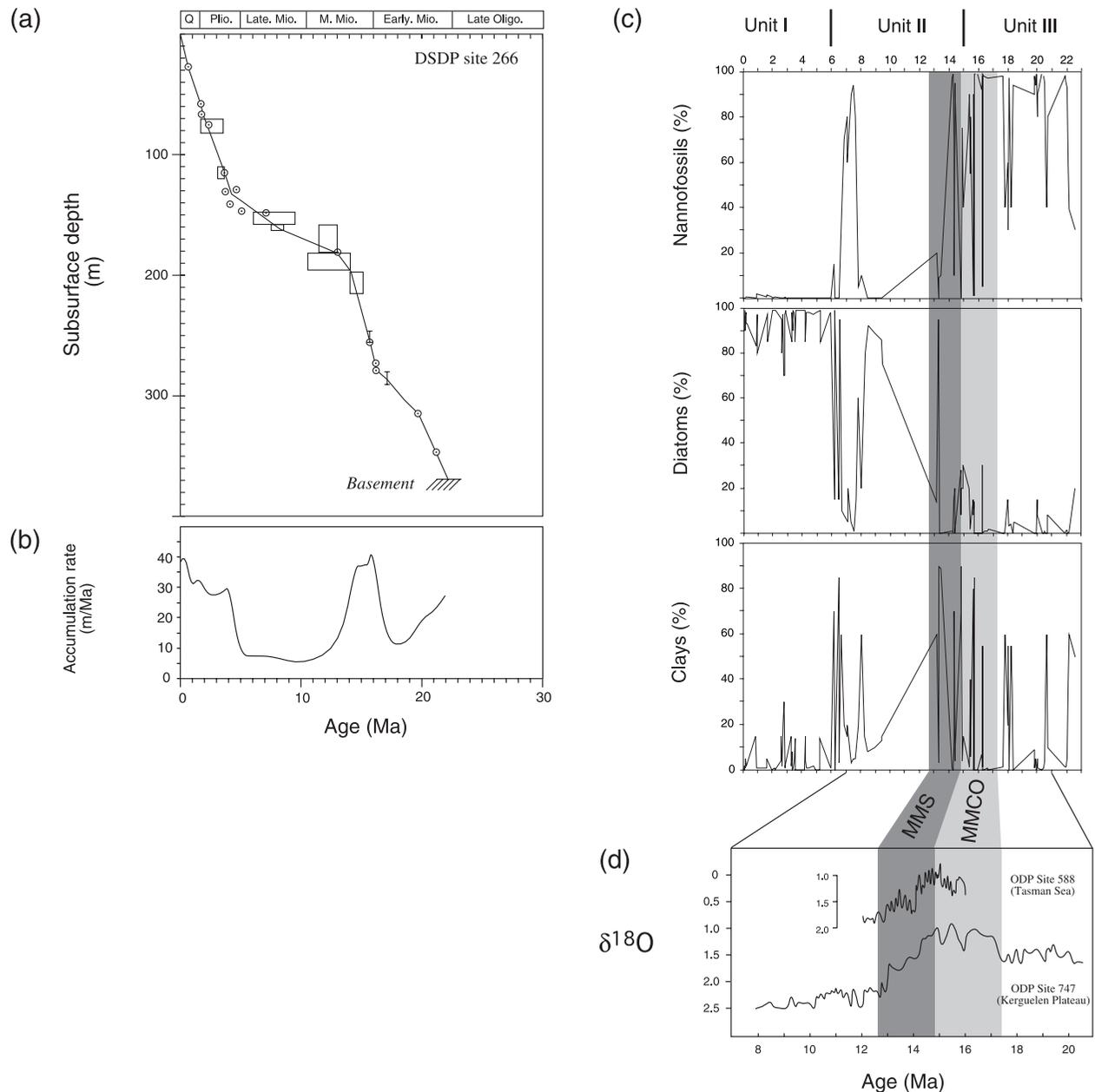
Figure 2. Previous results. (a) Age inferred using the indicated microfossil data versus depth at site 266 [from *Hayes et al.*, 1975]. (b) Inferred sedimentation rate. (c) Temporal variations of microfossil abundances at site 266 [from *Hayes et al.*, 1975]. (d) Oxygen isotope time series from nearby sediment cores: ODP site 747 (Kerguelen plateau, data from *Wright and Miller* [1992]) and ODP site 588 (Tasman Sea, data from *Flower and Kennett* [1993]). These data are used to identify the Middle Miocene Climatic Optimum (MMCO) from 17 to 15 Ma and the Middle Miocene Shift (MMS) from 15 to 12.5 Ma.

by a full chemical and isotopical characterization. Major elements were quantified by the "Service d'Analyse des Roches et des Minéraux" of the CRPG (Nancy) on an ICP-AES (Jobin-Yvon JY 70) using a lithium metaborate ($LiBO_2$) fusing technique. For trace elements and isotopic analysis, samples were dissolved in HNO_3-HF mixtures (1:5) in Teflon beakers. Complete dissolution was

assured by placing the beakers in steeled-jacked PARR bombs at 150°C for one week. Trace elements were measured by ICP-MS (VG PQ2+) at LGCA following a new procedure that was set up by Dimitri Ionov during his stay at LGCA. The improvements consist of: (1) diluting each sample in order to have the same elemental charge in the analyzed solutions (20 mg in

Table 1. Depth, Age, and Major Element Composition of Sediments From DSDP Site 266[a]

Core (Sample Name)	Depth, mbsf	Age, Ma	SiO_2	Al_2O_3	Fe_2O_3	MnO	MgO	CaO	Na_2O	K_2O	TiO_2	P_2O_5	Total
1	2.82	0.1	85.14	1.46	0.69	0.06	0.84	0.47	4.03	0.50	0.11	0.06	93.36
2	27.67	0.7	70.58	0.87	0.40	0.04	0.58	13.55	2.94	0.35	0.06	0.00	89.37
3	44.20	1.2	83.90	2.70	1.72	0.04	1.16	0.77	2.21	0.88	0.18	0.09	93.65
4	65.20	1.9	87.54	1.18	0.52	0.00	0.58	0.80	3.28	0.51	0.07	0.05	94.53
5	85.32	2.6	71.54	7.82	4.64	0.07	1.84	1.16	4.22	1.90	0.60	0.16	93.95
6	104.20	3.3	79.27	4.52	2.59	0.04	1.00	0.55	3.18	1.30	0.25	0.06	92.76
7	122.86	3.9	77.48	4.12	2.14	0.05	0.98	0.37	4.18	1.19	0.25	0.00	90.76
8	132.08	4.2	76.01	7.50	4.23	0.07	1.72	0.86	3.40	2.04	0.54	0.15	96.52
9	141.76	5.5	71.67	8.56	4.38	0.06	2.00	0.91	4.05	2.38	0.52	0.14	94.67
10	151.60	6.9	45.35	5.98	2.55	0.23	1.31	29.78	2.18	1.54	0.27	0.00	89.19
11	160.63	8.1	65.99	10.51	4.93	0.41	2.32	3.27	3.39	2.82	0.57	0.23	94.44
12	178.80	12.3	63.43	12.77	6.12	0.27	2.93	2.63	4.11	3.55	0.59	0.24	96.64
13	198.55	14.2	15.01	8.42	1.11	0.16	0.64	46.18	1.10	0.79	0.13	0.00	73.54
14	217.60	14.7	57.40	10.44	4.93	0.16	2.42	9.32	2.53	2.82	0.48	0.20	90.70
15	236.37	15.2	47.10	9.15	4.02	0.27	2.13	23.07	2.40	2.60	0.45	0.16	91.35
16	245.37	15.4	29.88	6.22	2.67	0.21	1.51	35.78	1.74	1.83	0.29	0.06	80.19
17	254.93	15.7	20.50	3.94	1.57	0.14	0.90	41.84	1.51	1.09	0.17	0.00	71.66
18	274.89	16.2	20.18	3.81	1.58	0.13	1.10	41.99	2.67	1.07	0.18	0.00	72.71
19	293.78	17.8	40.02	8.18	3.68	0.16	1.88	29.40	2.04	2.36	0.40	0.09	88.21
20	312.70	19.5	29.81	6.08	2.54	0.12	1.39	36.48	1.60	1.71	0.28	0.00	80.01
21	331.36	20.5	21.70	4.25	1.85	0.08	1.16	42.26	1.51	1.17	0.19	0.00	74.17
22	359.37	21.7	18.49	2.45	0.96	0.06	0.67	44.82	1.19	0.61	0.12	0.00	69.37

[a] Ages are from *Hayes et al.* [1975]. All concentrations are in wt. %. LOI was not measured because of the small quantity of sample available.

40 mL of HNO_3 2%) and, (2) monitoring within-run machine drift on a large mass band with a multispike (As, In, Tm). Signal calibration was made by repeatedly analyzing the BR standard, using for reference the values recommended by *Eggins et al.* [1997]. The accuracy and precision of the method were estimated by running repeatedly BHVO-1 standard as an unknown sample. The external precision of the method (2σ error) is <5% for most elements.

[8] Lead was separated and purified using an HNO_3-HBr procedure modified from *Lugmair and Galer* [1992]. During the study, the total procedural blank is <100 pg (n = 3) and is negligible compared to the amount of Pb extracted. Rare earth elements were separated on 2 mL Biorad columns filled with AG50-X8 cationic resin using HCl acid of increasing normality. Neodymium was extracted on Eichrom Ln resin using diluted HCl acid. The purification of Hf was accomplished using a procedure modified from *Blichert-Toft et al.* [1997] where the first step of separation (HF leaching and fluoride precipitation) was replaced by a pass on a high-capacity cationic resin (AG50-X12). Pb, Nd and Hf isotopic compositions were determined by MC-ICPMS (VG Plasma 54) at ENS Lyon. For Pb, a thallium 205–203 spike was used to monitor mass fractionation, as initially proposed by *Walder and Furuta* [1993]

and subsequently applied to this instrument by *White et al.* [2000]. A standard bracketing technique was used to correct machine drift. The external reproducibility of the Pb isotope measurements was estimated by measuring repeatedly (n = 12) an in-house standard (a Fe-Mn nodule from the Indian Ocean) and yielded 350 ppm (2σ) for ratios involving ^{204}Pb and 250 ppm (2σ) or less for other ratios. Nd and Hf external errors, as estimated from replicate analyses of standards and samples, are 0.5 and 0.6 epsilon unit (2σ), respectively.

4. Results

4.1. Major Elements (Table 1)

[9] Major element concentrations (Figures 3 and 4) show large and systematic variations that reflect the change in the lithology: SiO_2 increases and CaO decreases through time, showing a major shift at about 15 Ma. A positive CaO anomaly during the MMCO is superimposed on the smooth evolution. Corresponding negative anomalies are observed for other elements. Al_2O_3, together with other elements enriched in the detrital fraction (Fe_2O_3, MgO, K_2O or TiO_2), increase from 22 to ~12 Ma and decrease since then. Their abundances are inversely proportional to that of the biogenic
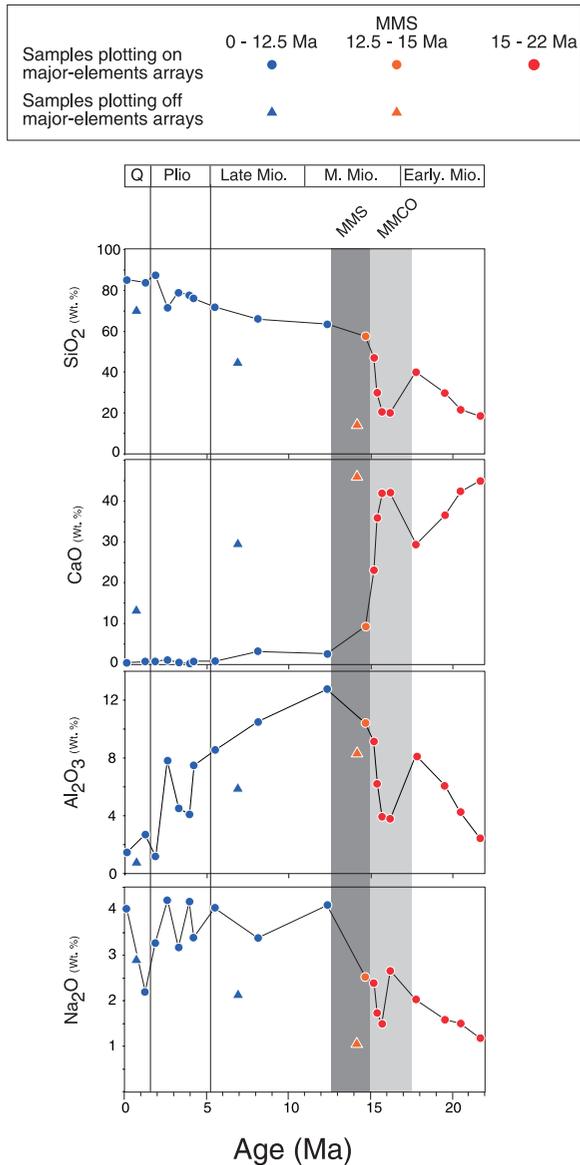
Figure 3. Selected major element concentrations plotted versus age. The Middle Miocene Climatic Optimum (MMCO) and subsequent Middle Miocene Shift (MMS) are indicated.

component. Na_2O correlates with Al_2O_3 before 15 Ma but not after. CaO correlates negatively with SiO_2 for samples having >1% of CaO and <70% of SiO_2. Al_2O_3 correlates positively with SiO_2 from 21.7 to 14.7 Ma and negatively afterward. Principal component analysis reveals a "V-shaped" pattern, which is essentially contained within a single plane (Figure 5). This remarkable feature has strong implications: (1) Mixing two biogenic components (siliceous and carbonaceous) with a single clay component can explain most of the major element variability, and (2) two binary

mixtures formed successively: clays are diluted in a $CaCO_3$ matrix before 14 Ma and in a biogenic SiO_2 matrix thereafter.

4.2. Trace Elements (Table 2)

[10] Rare earth element (REE) concentrations normalized to the average composition of depleted Mid-Ocean Ridge Basalts (MORB) show enriched patterns, with a systematic negative Eu anomaly (Figure 6). Normalizing the data to the upper continental crust composition reveals relatively flat distributions, with a slight enrichment of middle REE (Sm to Ho). For both normalizations, the Ce anomaly switches from negative to positive at about 14 Ma. When plotted versus time (Figure 7), trace element concentrations vary at first glance like Al_2O_3, showing a maximum near the MMS and a negative anomaly during the preceding MMCO. In detail, as suggested by the La versus Al_2O_3 relationship (Figure 4), the relative behaviors of the elements concentrated in clays seem to change at about 14 Ma. A synthesis of variations of trace element ratios (Figure 7) reveals that the MMS is recorded differently depending on the behavior of the elements during continental weathering and transport to the seafloor. Ratios involving elements with similar geochemical behaviors (Th/U, Zr/Hf, Nb/Ta) show surprisingly large variations, which are controlled by the abundance of the biogenic component. Ratios involving elements with different behaviors during weathering show an abrupt shift during the MMS (La/Nb, Rb/Sr) or a more progressive variation (Lu/Hf). Ratios involving an element that is highly reactive in seawater at the nominator, such as Pb/Nd or Ce/Nd, display a continuous increase during the Miocene.

4.3. Pb, Nd, and Hf Isotopes (Table 3)

[11] Isotope ratios display systematic variations when plotted versus time (Figure 8). $^{206}Pb/^{204}Pb$, $^{207}Pb/^{204}Pb$ and $^{208}Pb/^{204}Pb$ increase from the early Miocene to the end of the MMCO before decreasing during the MMS. The late Miocene is characterized by negligible $^{207}Pb/^{204}Pb$ and $^{208}Pb/^{204}Pb$ variations and a slight $^{206}Pb/^{204}Pb$ decrease. $^{20X}Pb/^{204}Pb$ ratios (x = 6, 7, 8) markedly decrease during the Pliocene and subsequently increase during the Quaternary. εNd increases from ~-13 to ~-10 through the Miocene, and oscillates between ~-10.5 and ~-7.5 during the last 5 Ma. εHf also displays a pronounced increase, from ~-10 during the Early and Middle Miocene to ~-1 during the Pliocene. Pb-Pb isotope relationships (Figure 9) show two
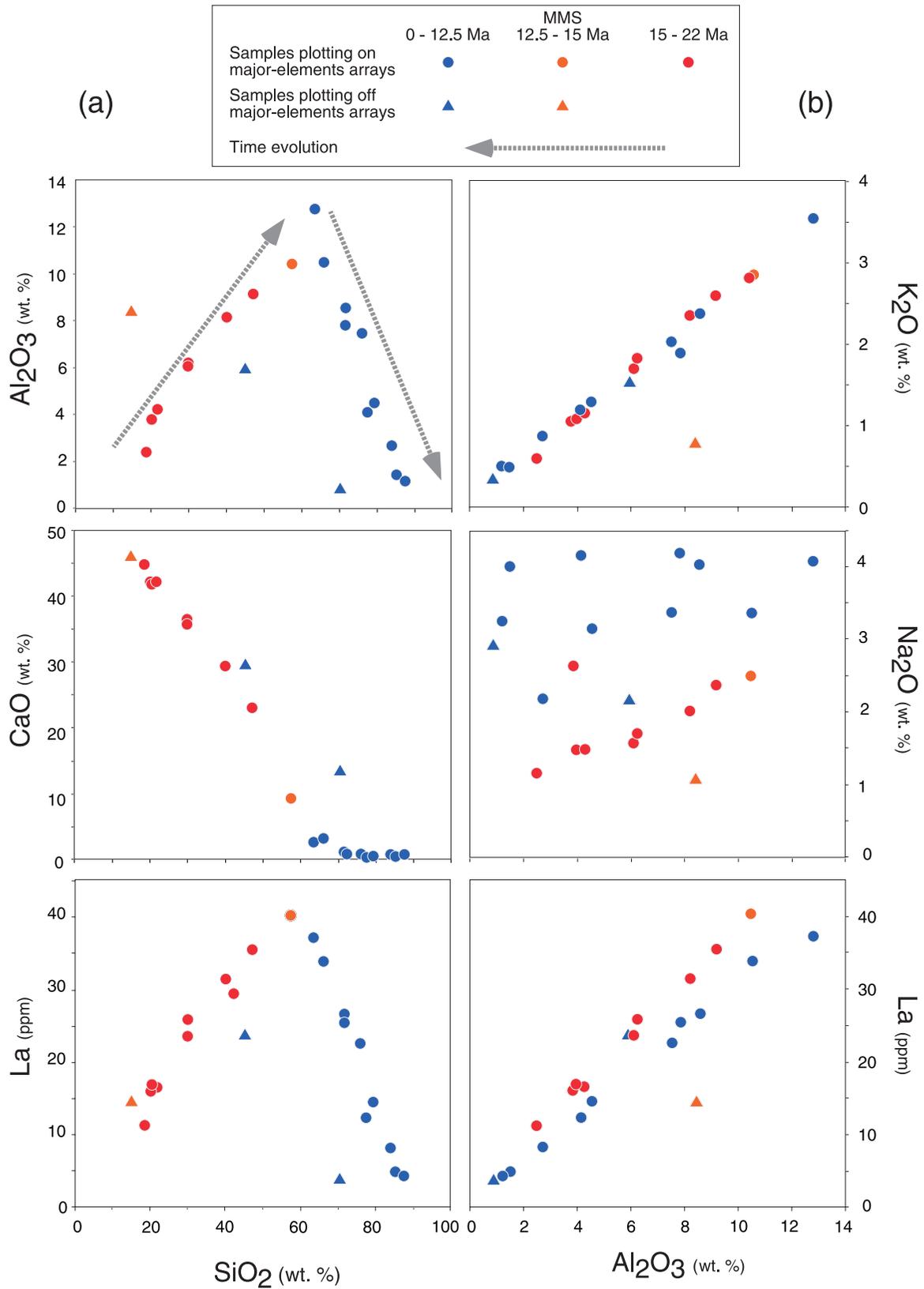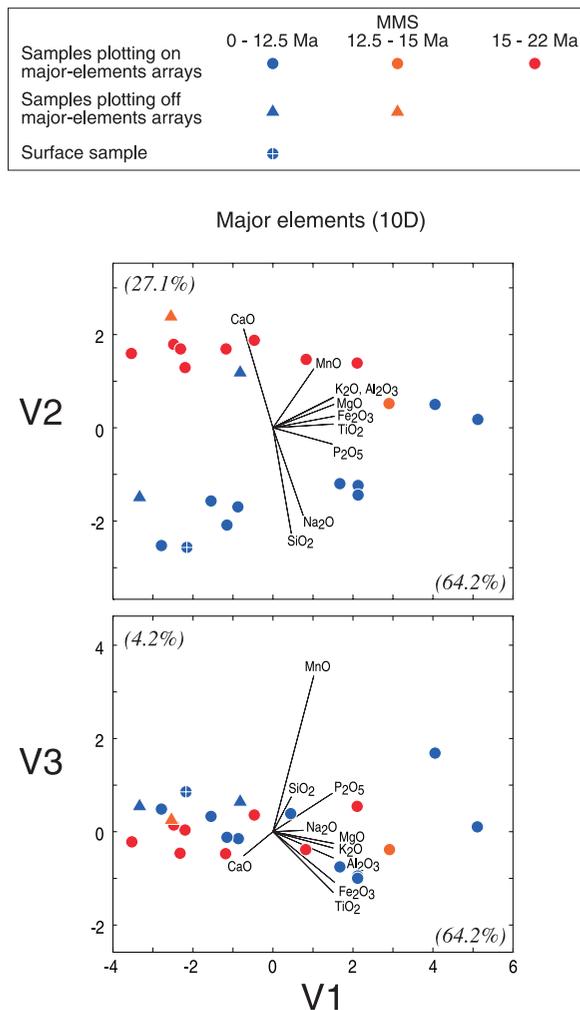
Figure 4. Selected major and trace elements plotted versus (a) SiO$_2$ and (b) Al$_2$O$_3$.

Figure 5. Principal component analysis (PCA) of the major element data set. Dispersion is here quantified by variances. The V1 axis gives the first "principal component" which is the most dispersive direction. The second principal component, V2, is the most dispersive direction perpendicularly to V1. Combining V2 with V1 projections (upper plot) shows the "plane view". The third principal component, V3, is the most dispersive direction perpendicularly to V1 and V2. Combining V3 with V1 projections (lower plot) shows a "thickness view". The chosen units are the classical standard deviations of the data (PCA on correlation matrices). Note that the use of raw geochemical units (concentrations) does not change significantly the results. Percentages given along with the axis names are the fractions of total variance each principal axis accounts for. The plane view (upper plot) accounts for 91.3% revealing a spatial variability of the data cloud mostly in two dimensions. The projections of individual geochemical axis are shown (vectors of length 4 units). The nearer to 4 the length of a projected vector, the more parallel to the projection plane this direction is. Samples plotting off major element correlations (triangles) have not been used in calculating PCA but are nevertheless shown.

main arrays corresponding to the 22–15 and 15–2 Ma time periods. The two samples from the Pleistocene (0.7 and 1.2 Ma) plot clearly below these arrays in $^{208}Pb/^{204}Pb$ versus $^{206}Pb/^{204}Pb$ space, possibly defining a third array, whereas the subsurface sample plots within the 15–2 Ma array. εNd correlates with εHf (r = 0.70), and they both correlate with $^{207}Pb/^{204}Pb$ (r = 0.62 and 0.50, respectively) and $^{208}Pb/^{204}Pb$ (r = 0.51 and 0.40, respectively) but not with $^{206}Pb/^{204}Pb$ (r = 0.11 and 0.13, respectively).

4.4. Trace Element Ratios Versus Time-Integrated Ratios

[12] The absence of correlation between isotopic ratios and corresponding parent-daughter ratios (Figure 10) indicates that trace element ratios have not been recorded by isotopes, and thus necessarily reflect postdepositional sedimentary processes. In support of this idea, the relation between measured Th/U and time-integrated Th/U (κ^* estimated from radiogenic $^{208}Pb/^{206}Pb$) indicates that Th/U variations do not predate sediment deposition. Consequently, trace element ratios may not be appropriate to discuss elemental sources.

5. Discussion

### 5.1. Isotopes Versus Lithology

[13] A major result of this study is the identification of systematic variation through time of the isotopic composition of sediments at site 266, a variation that may be interpreted as reflecting a change of sediment provenance during the Miocene. However, because the isotopic analyses have been performed on bulk sediments, the possibility that the isotopic variations reflect changes in sediment lithology should first be considered. To answer this question, one needs to know (1) the phases that concentrate the trace elements of interest (Pb, Nd and Hf) and (2) the relative abundance of these phases and their fluctuations along the sediment core. Constraints on trace element bearing phases may be obtained from major and trace element relationships. Pb, Nd and Hf correlate strongly with Al_2O_3, K_2O, Fe_2O_3, MgO and TiO_2, but weakly with MnO and P_2O_5 (not shown), suggesting that their abundance in sediments is dominantly controlled by the clay fraction, rather than by a biogenic or an Mn oxide phase. However, neither Pb nor Nd and Hf isotopic ratios significantly correlate with the abundance of the clay fraction. These observations

Table 2. Trace Element Composition of Sediments From DSDP Site 266[a]

Sample	Age, Ma	Duplicates	Rb	Sr	Y	Zr	Nb	Ba	La	Ce	Pr	Nd	Sm	Eu	Gd	Tb	Dy	Ho	Er	Yb	Lu	Hf	Ta	Pb	Th	U
1	0.1		18.5	82	3.72	36.3	4.06	1248	4.96	11.85	1.11	4.04	0.71	0.20	0.77	0.10	0.54	0.11	0.34	0.28	0.05	0.68	0.25	2.98	1.82	0.56
2	0.7		10.3	390	5.03	26.8	2.30	1240	3.92	8.22	0.89	3.38	0.66	0.17	0.72	0.10	0.59	0.13	0.39	0.37	0.06	0.49	0.14	3.13	1.13	0.83
3	1.2		30.4	106	6.79	55.2	6.64	1628	8.32	21.55	2.02	7.51	1.44	0.30	1.30	0.18	1.08	0.20	0.60	0.54	0.09	1.19	0.43	10.98	3.26	0.55
4	1.9		26.3	71	3.40	23.2	2.28	914	4.42	10.96	1.01	3.60	0.67	0.16	0.61	0.10	0.50	0.11	0.37	0.30	0.04	0.44	0.14	2.59	1.70	0.44
5	2.6	DD	70.7	180	18.00	152.7	20.58	1921	25.54	64.22	6.13	22.45	4.23	0.92	3.63	0.55	3.04	0.60	1.59	1.46	0.22	3.47	1.30	16.73	9.09	1.05
6	3.3		51.8	124	10.39	88.5	10.52	2742	14.61	39.80	3.41	12.24	2.31	0.49	2.10	0.30	1.63	0.33	0.97	0.86	0.14	1.84	0.70	9.33	5.89	0.87
7	3.9		45.3	120	9.06	84.0	11.13	1688	12.42	33.01	2.97	10.57	2.02	0.46	1.80	0.26	1.42	0.27	0.83	0.71	0.11	1.82	0.71	9.53	4.89	1.72
8	4.2		73.2	181	15.77	137.1	19.19	2700	22.68	59.78	5.50	19.92	3.69	0.84	3.39	0.47	2.65	0.52	1.38	1.31	0.21	3.06	1.26	16.31	8.66	1.03
9	5.5		94.7	177	19.67	136.7	18.07	2708	26.67	68.56	6.53	23.86	4.42	0.90	3.72	0.56	3.20	0.61	1.73	1.59	0.25	3.16	1.19	17.21	10.55	1.06
10	6.9	DR	68.7	1164	23.11	75.6	9.29	2164	23.75	42.79	5.91	22.50	4.41	0.95	4.26	0.60	3.43	0.67	1.82	1.55	0.24	1.75	0.60	10.77	7.70	0.72
11	8.1	DR	120.5	269	29.73	134.9	16.84	2270	33.96	77.69	8.71	32.55	6.41	1.35	5.69	0.86	4.79	0.96	2.62	2.31	0.36	3.25	1.12	20.26	13.64	1.31
12	12.3		123.1	204	37.45	152.2	18.54	2351	37.27	89.75	9.91	37.33	7.63	1.53	6.79	1.04	6.08	1.20	3.25	2.99	0.45	3.67	1.23	22.98	17.36	1.40
13	14.2		35.9	1934	15.05	37.5	3.92	1505	14.65	24.68	3.51	13.14	2.58	0.56	2.39	0.35	2.13	0.42	1.16	1.07	0.16	0.82	0.26	5.85	4.00	0.30
14	14.7		137.2	609	36.11	133.9	13.94	3711	40.38	83.17	10.02	36.87	7.28	1.51	6.71	0.96	5.63	1.17	3.33	3.00	0.45	3.33	0.96	19.78	16.77	1.29
15	15.2		85.7	949	32.15	106.1	11.45	4361	35.59	68.47	8.90	34.46	6.77	1.46	6.79	0.93	5.30	1.10	3.08	2.74	0.43	2.77	0.81	14.37	12.49	1.24
16	15.4		78.9	1521	24.87	75.1	7.88	2870	25.94	47.92	6.53	24.92	4.75	1.05	4.64	0.66	3.78	0.78	2.15	1.94	0.30	1.87	0.52	11.58	9.41	0.72
17	15.7		44.0	1807	17.71	48.2	5.30	1413	17.06	30.78	4.44	16.87	3.26	0.66	2.92	0.45	2.55	0.53	1.52	1.33	0.21	1.14	0.34	8.94	2.37	0.60
18	16.2		39.1	1639	11.35	38.8	5.07	1290	16.22	27.82	3.96	15.11	2.83	0.60	2.60	0.36	2.08	0.43	1.17	1.00	0.16	0.87	0.32	7.53	0.75	0.44
19	17.8		98.8	1175	27.15	94.6	10.45	2015	31.60	64.87	7.67	28.45	5.46	1.10	5.02	0.74	4.21	0.85	2.42	2.17	0.33	2.29	0.70	11.87	11.61	0.90
20	19.5	DD	72.2	1548	21.57	74.9	8.01	1682	23.65	45.83	5.85	22.29	4.30	0.87	3.63	0.57	3.36	0.66	1.85	1.68	0.25	1.80	0.52	7.97	8.46	0.89
21	20.5		40.3	1629	14.52	46.5	5.91	1150	16.65	28.63	4.24	16.27	3.08	0.63	2.83	0.40	2.40	0.48	1.34	1.16	0.18	1.06	0.37	5.36	1.86	0.46
22	21.7		27.1	1362	10.36	30.3	3.16	1740	11.32	16.68	2.77	10.58	2.07	0.46	2.04	0.28	1.64	0.34	0.92	0.81	0.12	0.60	0.20	3.24	0.56	0.30
BHVO-1	n = 11		10.45	430	29.43	187.6	21.1	142.1	16.27	39.45	5.64	25.48	6.10	2.01	5.90	0.93	5.22	0.98	2.53	1.97	0.28	4.31	1.20	2.02	1.29	0.41
	2σ		4.1	4.9	3.5	3.4	4.4	6.5	6.2	5.1	3.2	2.4	2.0	4.5	3.7	2.6	2.9	1.7	1.7	4.5	4.8	4.6	5.2	4.6	5.9	6.8

[a] All data are relative to the BR standard [Eggins et al., 1997]. All data are in ppm. DR, duplicate run; DD, duplicate dissolution.
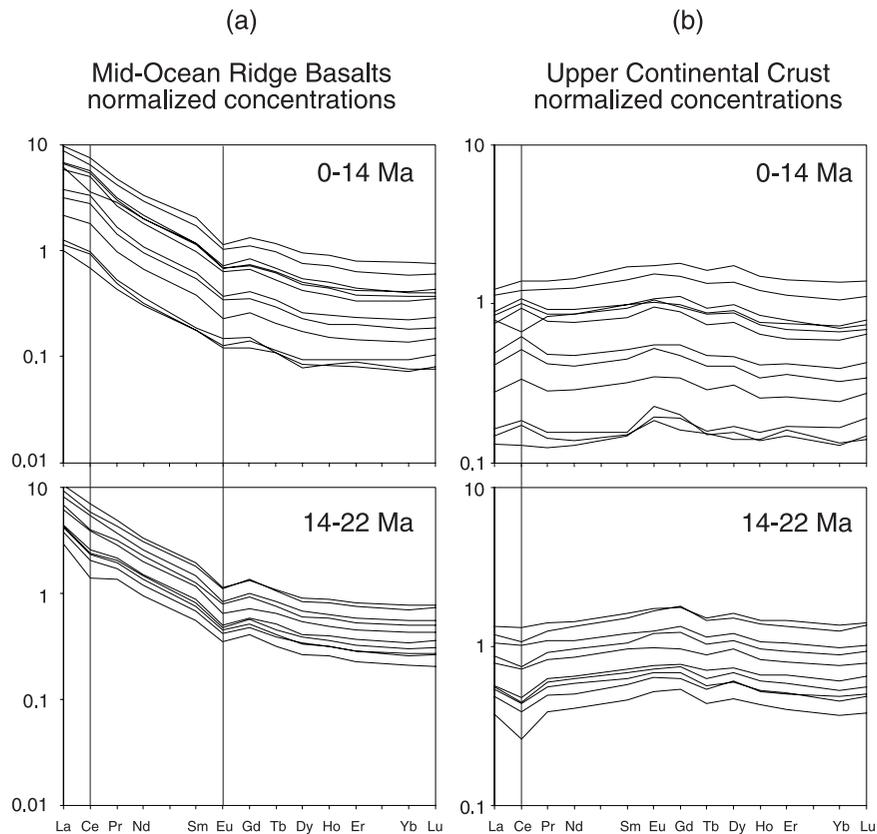
Figure 6. Rare earth elements normalized to the average composition of (a) depleted Mid-Ocean Ridge Basalts [*Hofmann*, 1988] and (b) upper continental crust [*McLennan*, 2001].

strongly suggest that the isotopic variations of the bulk sediment reflect a change in clay provenance rather than changes in the relative proportions of sediment phases.

5.2. Elemental Sources

[14] Previous geochemical studies have proposed that the detrital sediments deposited in the Australian-Antarctic basin are mixtures between inputs from the Kerguelen-Crozet volcanic province and inputs from the Antarctic continent [*Bareille et al.*, 1994; *Dezileau et al.*, 2000; *Joseph et al.*, 2002]. The Nd-Hf isotopic variations at site 266 may also reflect mixing between these two sources (Figure 11), although a seawater contribution is required to explain why the data plot slightly above the terrestrial array.

[15] Pb isotope systematics are more complex and require the mixing of at least four components (Figure 12): (1) Detrital sediments from the Antarctic continent having low-^{206}Pb/^{204}Pb, high ^{207}Pb/^{204}Pb and ^{208}Pb/^{204}Pb. (2) Detrital sediments from a basaltic source having low ^{206}Pb/^{204}Pb and ^{207}Pb/^{204}Pb, and intermediate ^{208}Pb/^{204}Pb. The

eastward decrease of ^{87}Sr/^{86}Sr observed within the Australian-Antarctic basin [*Bareille et al.*, 1994] suggests that the dominant basaltic source in the area is the Kerguelen plateau rather than the SEIR. (3) Dissolved unradiogenic Pb derived from hydrothermal systems. (4) Dissolved radiogenic Pb. The origin of the latter component, whose ^{208}Pb/^{204}Pb is remarkably high, has been the object of debate. *Abouchami and Goldstein* [1995] suggested advection of Atlantic-derived Pb, whereas *Vlastélic et al.* [2001] subsequently proposed a regional deepwater source, such as the Weddell Sea or the Ross Sea. The composition of this component, which is best represented by the intersection of the two main Pb-Pb arrays (^{206}Pb/^{204}Pb = ~19.30; ^{207}Pb/^{204}Pb = ~15.72; ^{208}Pb/^{204}Pb = ~39.83), is similar to estimates of average upper continental crust [*Asmerom and Jacobsen*, 1993; *Hemming and McLennan*, 2001; *Millot et al.*, 2004], albeit with slightly lower ^{207}Pb/^{204}Pb and higher ^{208}Pb/^{204}Pb (Figure 12). This observation strongly suggests that this component originates from Antarctica. Antarctica terrains are similar in age and composition to other continents of the southern hemisphere, with the exception of the oldest, possibly
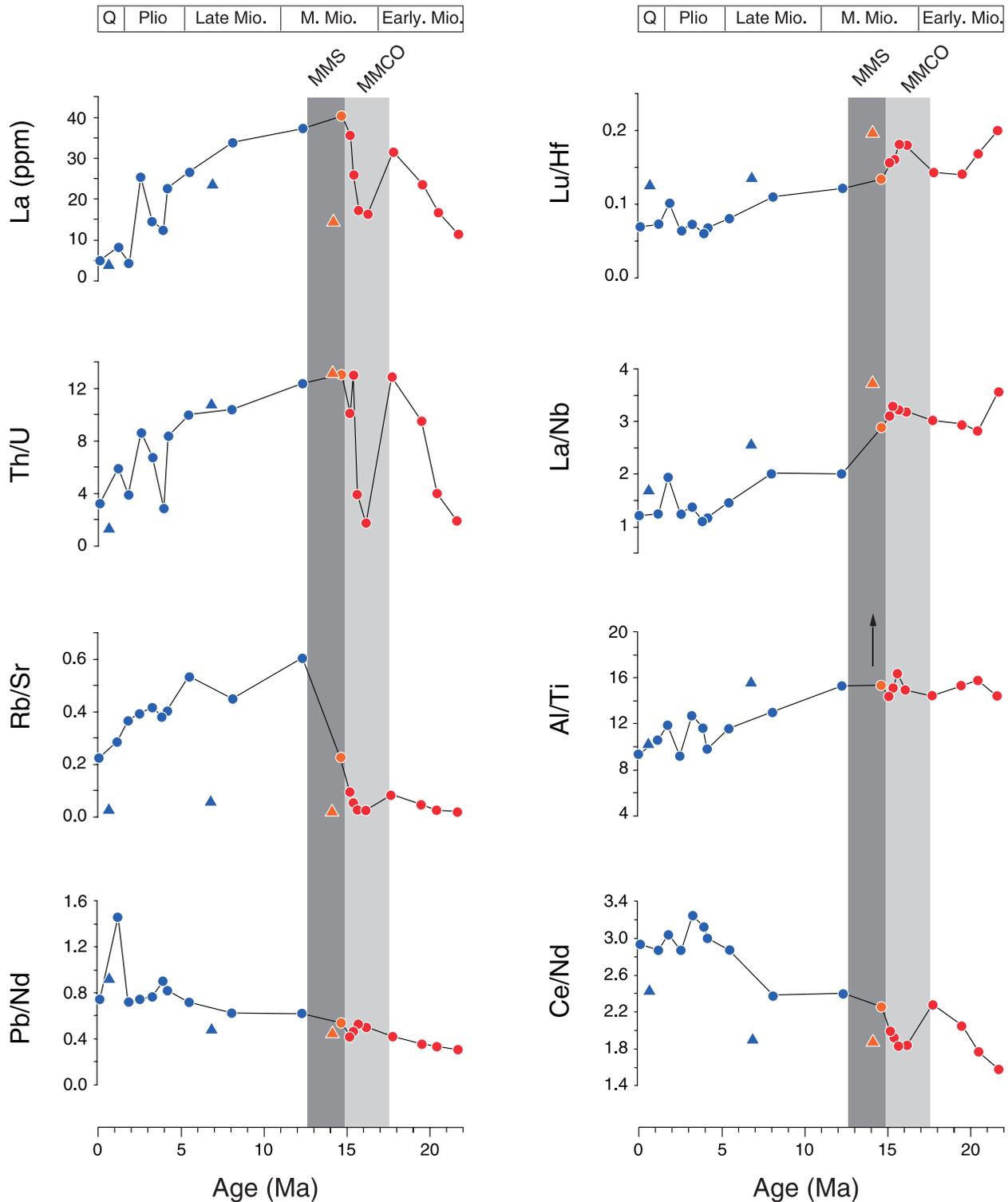
Figure 7. Selected trace element and trace element ratios plotted versus time. The Al/Ti ratio is also shown. Arrow is for out-of-scale data point.

Archean units exposed in East Antarctica (i.e., the Sverdrupfjella), which have distinctively high $^{208}Pb/^{204}Pb$ relative to the reference Pb growth curve [*Wareham et al.*, 1998; *Hoch et al.*, 2001].

Most Pb isotopic compositions from Antarctica published in the literature have been determined on plagioclase or potassium feldspar, which have low U/Pb and Th/Pb and thus preserve a "common

Table 3. Pb, Nd, and Hf Isotope Composition of Sediments From DSDP Site 266[a]

Sample	Age, Ma	Duplicates	$^{206}Pb/^{204}Pb$	$^{207}Pb/^{204}Pb$	$^{208}Pb/^{204}Pb$	$^{143}Nd/^{144}Nd$	$\epsilon Nd (T)$[b]	$^{176}Hf/^{177}Hf$	$\epsilon Hf (T)$[c]
1	0.1	DR (Pb)	18.847	15.661	39.255	0.512167	−9.18		
2	0.7		18.793	15.653	38.932	0.512265	−7.28		
3	1.2	DR (Pb)	18.693	15.636	38.751	0.512251	−7.53	0.282764	−0.25
4	1.9		18.743	15.653	39.095	0.512087	−10.73		
5	2.6	DD, DR (Pb, Nd)	18.829	15.656	39.204	0.512244	−7.65		
6	3.3		18.821	15.661	39.165	0.512139	−9.71	0.282733	−1.31
7	3.9		18.825	15.659	39.145	0.512241	−7.70	0.282733	−1.31
8	4.2		18.876	15.669	39.196				
9	5.5	DR (Nd)	18.844	15.670	39.265	0.512079	−10.84		
10	6.9		18.820	15.659	39.096	0.512231	−7.87	0.282612	−5.59
11	8.1	DR (Nd)	18.922	15.670	39.268	0.512141	−9.62	0.282734	−1.26
12	12.3	DD (Hf), DR (Nd)	18.874	15.673	39.238	0.512060	−11.15	0.282573	−6.90
13	14.2	DR (Pb)	19.000	15.684	39.394	0.512055	−11.23		
14	14.7	DR (Nd)	18.936	15.678	39.327	0.511985	−12.59	0.282465	−10.73
15	15.2	DR (Pb)	18.786	15.676	39.216	0.512003	−12.23		
16	15.4		18.943	15.690	39.400	0.511998	−12.32		
17	15.7		18.957	15.687	39.414	0.512041	−11.49	0.282581	−6.67
18	16.2		18.913	15.685	39.388	0.512024	−11.81		
19	17.8		18.830	15.679	39.343	0.511944	−13.35	0.282507	−9.22
20	19.5	DD (Pb, Nd), DR (Nd)	18.794	15.675	39.288	0.512005	−12.14		
21	20.5		18.737	15.665	39.183	0.512005	−12.14	0.282563	−7.24
22	21.7		18.807	15.676	39.315				

[a] All isotopic compositions were acquired by MC-ICPMS (VG Plasma 54 at ENS Lyon). Pb isotopic ratios are relative to *Todt et al.* [1996] estimates for NBS 981 ($^{206}Pb/^{204}Pb$ = 16.9356, $^{207}Pb/^{204}Pb$ = 15.4891, and $^{208}Pb/^{204}Pb$ = 36.7006). Nd isotopic ratios are relative to Nd JMC ($^{143}Nd/^{144}Nd$ = 0.51214). Hf isotopic ratios are relative to Hf JMC 475 ($^{176}Hf/^{177}Hf$ = 0.28216). DD, duplicate dissolution; DR, duplicate run.

[b] $\epsilon Nd(T) = [(^{143}Nd/^{144}Nd)T_{sample}/(^{143}Nd/^{144}Nd)T_{CHUR} - 1].10^4$ with $(^{143}Nd/^{144}Nd)T = (^{143}Nd/^{144}Nd)0 - (^{147}Sm/^{144}Nd).(e^{\lambda 147 \cdot t} - 1)$, $(^{147}Sm/^{144}Nd)_{sample} = 0.60465.(Sm/Nd)_{sample}$, $(^{147}Sm/^{144}Nd)_{CHUR} = 0.1967$, $(^{143}Nd/^{144}Nd)0_{CHUR} = 0.512638$.

[c] $\epsilon Hf(T) = [(^{176}Hf/^{177}Hf)T_{sample}/(^{176}Hf/^{177}Hf)T_{CHUR} - 1].10^4$ with $(^{176}Hf/^{177}Hf)T = (^{176}Hf/^{177}Hf)0 - (^{176}Lu/^{177}Hf).(e^{\lambda 176 \cdot t} - 1)$, $(^{176}Lu/^{177}Hf)_{sample} = 0.142.(Lu/Hf)_{sample}$, $(^{176}Lu/^{177}Hf)_{CHUR} = 0.0332$, $(^{176}Hf/^{177}Hf)0_{CHUR} = 0.282772$.

lead" signature. These depleted minerals can be the source of unradiogenic Pb for the oldest sediments (15–22 Ma) (these data are not shown because most of them plot outside the frame of Figure 12). Secondary minerals in granites (such as biotite, apatite or monazite) have higher U/Pb and Th/Pb and thus develop more radiogenic Pb signatures through time. Despite the absence of data on such phases from Antarctica, some observations suggest that they may represent the high-$^{206}Pb/^{204}Pb$ source common to all sediments and nodules of the area: (1) During granitoid weathering, Pb is preferentially released from the accessory, radiogenic phases [*Erel et al.*, 1994; *Harlavan et al.*, 1998]. According to that process, the erosion products delivered to the Ocean are radiogenic fluids and unradiogenic detrital minerals. (2) Pb-Pb arrays in sediments are subparallel to the experimental vector that links residual minerals to the extracted leach [*Harlavan and Erel*, 2002] (Figure 13). (3) Preferential release of radiogenic Pb during continental weathering has been previously invoked to account for the signature of NADW [*von Blanckenburg and Nägler*, 2001].

[16] Despite the complexity inherent to four-component mixing, simple inferences can be made. The dominant source of low-$^{206}Pb/^{204}Pb$ lead is most likely detrital minerals (residual phases) delivered by Antarctica before 15 Ma and erosion of the Kerguelen basaltic province thereafter. Alternatively, an increased contribution of unradiogenic dissolved Pb may also have contributed to the observed isotopic shift. Such a contribution is required to explain the signature of the subsurface samples (0.7–1.2 Ma), which have anomalously low $^{208}Pb/^{204}Pb$. Seawater is also expected to be the source of high-$^{206}Pb/^{204}Pb$ lead. Altogether, these observations bring up the question about the total contribution of dissolved Pb (radiogenic + unradiogenic components). Following the approach of *Murray and Leinen* [1993], it can be estimated that the contribution of seawater-derived Pb (or detrital unsupported) increases from ∼30 to ∼60% upward the sediment column, reaching a maximum (∼80%) for the above mentioned subsurface samples. Such an increase may be linked to the higher proportion of highly particle-reactive clays, such as montmoril-
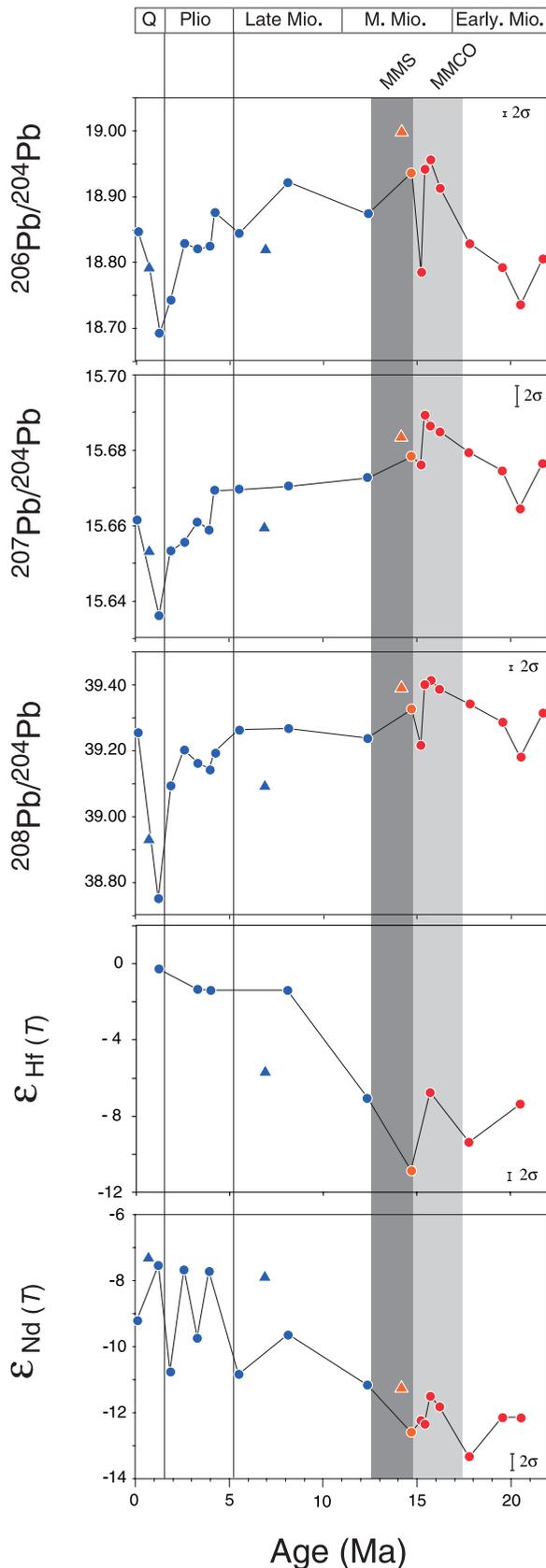
Figure 8. Isotope ratios plotted versus time. Age-corrected Nd and Hf ratios are shown (see Table 3).

lonite, toward the top of the sediment column [*Hayes et al.*, 1975]. Montmorillonite may also be responsible for the temporal increase of Pb/Nd and Ce/Nd ratios, as well as Na_2O concentration. In addition, considering that montmorillonite is probably an alteration product of basaltic debris in contact with seawater [*Piper*, 1974], its temporal increase is also consistent with the inferred change of the source of detrital material.

5.3. Mixing Model

[17] Pb, Nd and Hf isotopic variations of bulk sediments are most easily explained by mixing between a variable detrital component and seawater. These variations will accurately record fluctuations of the detrital signal only if both the elemental fraction derived from seawater and the isotopic composition of seawater have remained
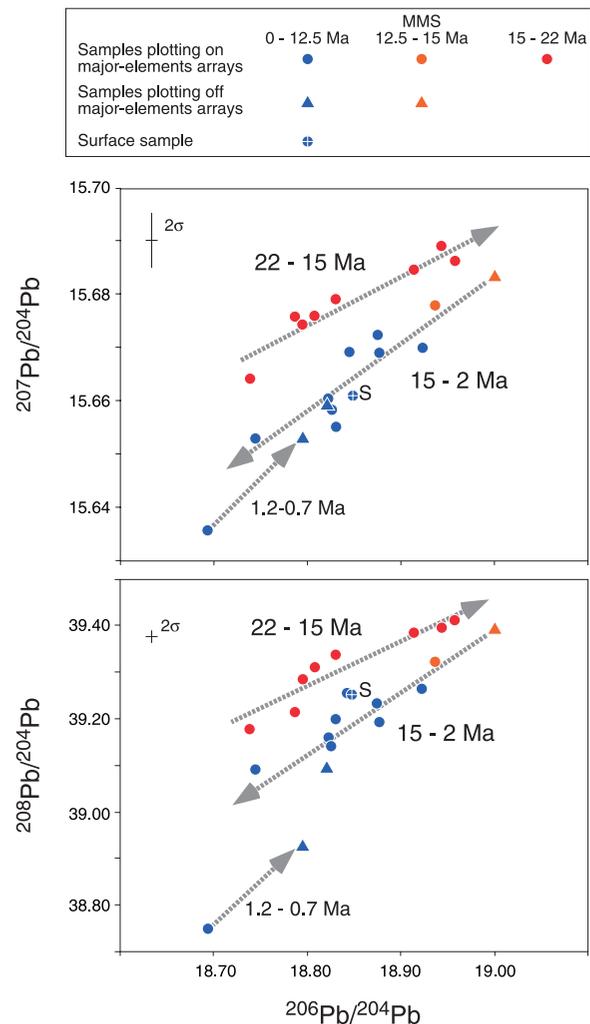
Figure 9. Pb-Pb plots. Arrows indicate main temporal trends.
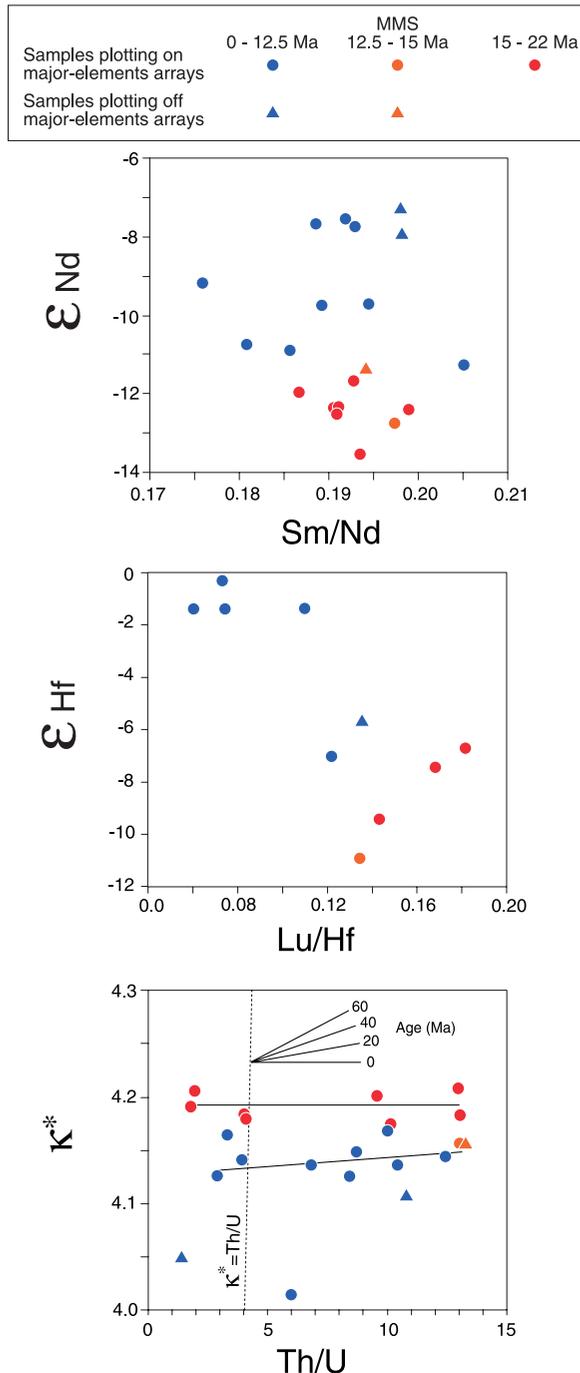
Figure 10. Trace element ratios versus time-integrated ratios. κ^* represents the Th/U ratio integrated by $^{208}Pb/^{206}Pb$ since 4.55 Ga [*Allègre et al.*, 1986]. The geochron ($\kappa^* = Th/U$) and some isochrons (20, 40, and 60 Ma) are shown. The absence of correlation between κ^* and Th/U indicates that Th/U variations at site 266 are recent (<20 Ma).

constant through time. This is possibly the case for Nd and Hf, because the isotopic composition of the Southern Indian Ocean has remained remarkably constant since the early Miocene [*O'Nions et al.*,

1998; *Piotrowski et al.*, 2000]. Pb isotopes are more problematic because the composition of both dissolved (seawater) and detrital lead has changed through time. Modeling in three-dimension lead isotopic space theoretically offers the possibility to resolve the temporal changes of the proportion of the four end-components, providing that the composition of each end-component is known accurately, which is not the case. Instead, in a simpler approach, the variations of $^{207}Pb/^{204}Pb$ at a given value of $^{206}Pb/^{204}Pb$ are assumed to record a detrital signal. The parameter used (($^{207}Pb/^{204}Pb)_{18.70}$) reflects the variations of $^{207}Pb/^{204}Pb$ at $^{206}Pb/^{204}Pb$ = 18.70 and has been obtained as explained in Figure 14 caption. Figure 14a not only emphasizes the drastic decrease of ($^{207}Pb/^{204}Pb)_{18.70}$ at 15 Ma, but also reveals remarkable similarities between ($^{207}Pb/^{204}Pb)_{18.70}$, εNd, and Al/Ti temporal variations, which reinforce the idea that these parameters reliably record a detrital signal. Change of the detrital source has been quantified independently using Nd isotopes and Al/Ti (Figures 14b and 14c). The two models agree well, given the uncertainties relative to the end-component compositions and the different sets of assumption used. Both models suggest a 30–40% reduction of Antarctic input and an equivalent increase of Kerguelen input during the Miocene. The proportions calculated for the surface sediment (~40% of Kerguelen material) are in total agreement with the proportions predicted at this longitude by *Bareille et al.* [1994].

5.4. Relation With Miocene Climate Change

[18] Miocene climate change has been extensively documented using stable isotopic records that show the succession of a warming trend (early Miocene), a climatic optimum (17–15 Ma) and a steep cooling trend (15–12.5 Ma). Site 266 sediment pile has reliably recorded this climate change, as illustrated by the middle Miocene transition from carbonaceous to bio-silica sedimentation and the pronounced carbonate spike at 15–17 Ma (Figure 3). In this section we discuss how the geochemical variations seen at site 266 can be linked to middle Miocene climate change and related events.

5.4.1. Antarctic Glaciation

[19] The influence of Antarctic glaciation on erosion rate and sediment transport is complex [*Hallet et al.*, 1996]. According to *Joseph et al.*
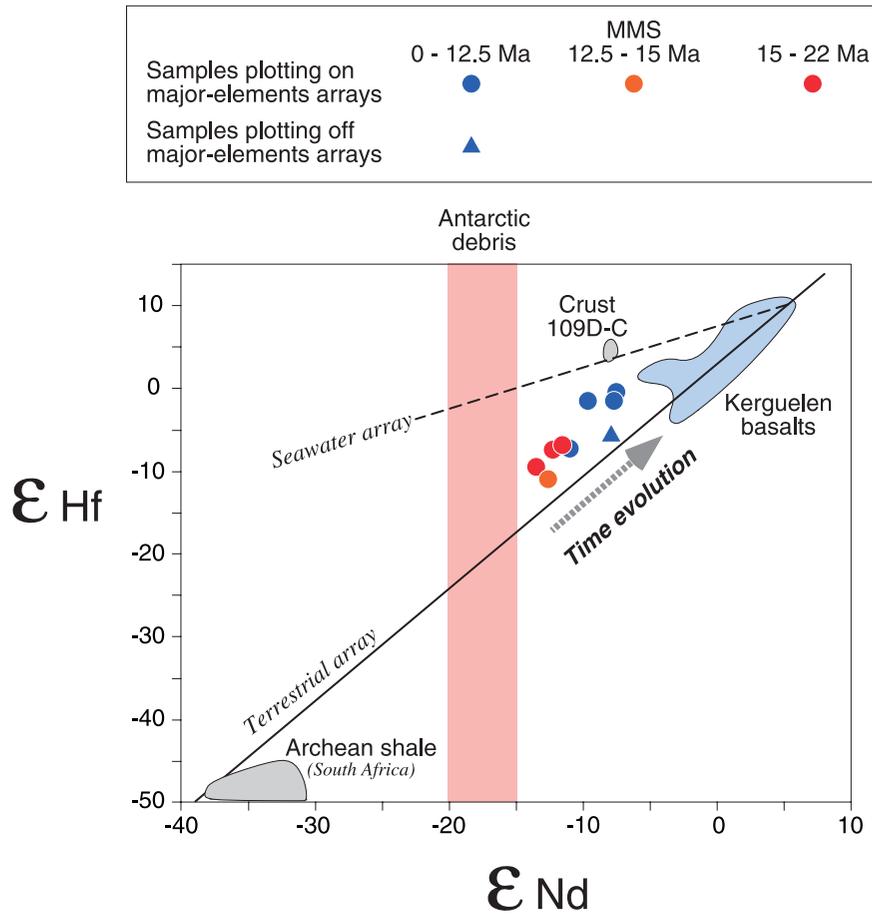
Figure 11. Plot of εHf versus εNd. Terrestrial [*Vervoort et al.*, 1999] and seawater [*Albarède et al.*, 1998] arrays are shown. Seawater composition over the last 22 Ma in the south Indian Ocean (Madagascar basin) is inferred from Fe-Mn crust 109D-C [*O'Nions et al.*, 1998; *Piotrowski et al.*, 2000]. The signatures of potential source rocks are also plotted: South African Archean shale [*Vervoort et al.*, 1999]; Antarctic debris recovered from ODP site 745 in the southeast Kerguelen plateau (only Nd data are given by *Joseph et al.* [2002]); Kerguelen basalts (MPI Georoc database, http://georoc.mpch-mainz.gwdg.de/georoc/).

[2002], Antarctic sediment supply to the Southern Ocean is reduced in the presence of a stable, cold-based East Antarctic ice sheet, but enhanced when the ice cover is active and wet-based. Site 266 isotopic data record a reduction of Antarctic input during the Miocene, and provide evidence for the formation of a stable, cold-based East-Antarctic ice sheet during this period. Additional constraints on the weathering processes taking place on Antarctica during the Miocene may be placed from Pb isotopes. At first glance, Pb isotope systematics of bulk sediments are complex because they require mixing of four distinct components, two of which most likely originating from seawater. However, simple inferences can be made considering that one component (Antarctic leach) predominantly controls the $^{206}Pb/^{204}Pb$ ratio of bulk sediments (this is because only that component has high

$^{206}Pb/^{204}Pb$; see Figure 12). Thus, in a first approximation, $^{206}Pb/^{204}Pb$ of bulk sediment may be used to infer the changes of seawater composition resulting from dissolved inputs from Antarctic continent. According to Figure 8, the inputs of radiogenic Pb from Antarctica followed climate change and reached a maximum during the MMCO. Two different processes may have operated: (1) Variable production of deep water (Antarctic Bottom Water, or AABW) near the Antarctic margin could have controlled the amount of radiogenic Pb from Antarctica transferred to the seafloor. This explanation is unlikely because there is no evidence for enhanced AABW production during the MMCO (see next section). (2) Enhanced chemical weathering of Antarctic granite could have preferentially released radiogenic Pb to the ocean [*Erel et al.*, 1994; *Harlavan and Erel*, 2002]. Such a process would
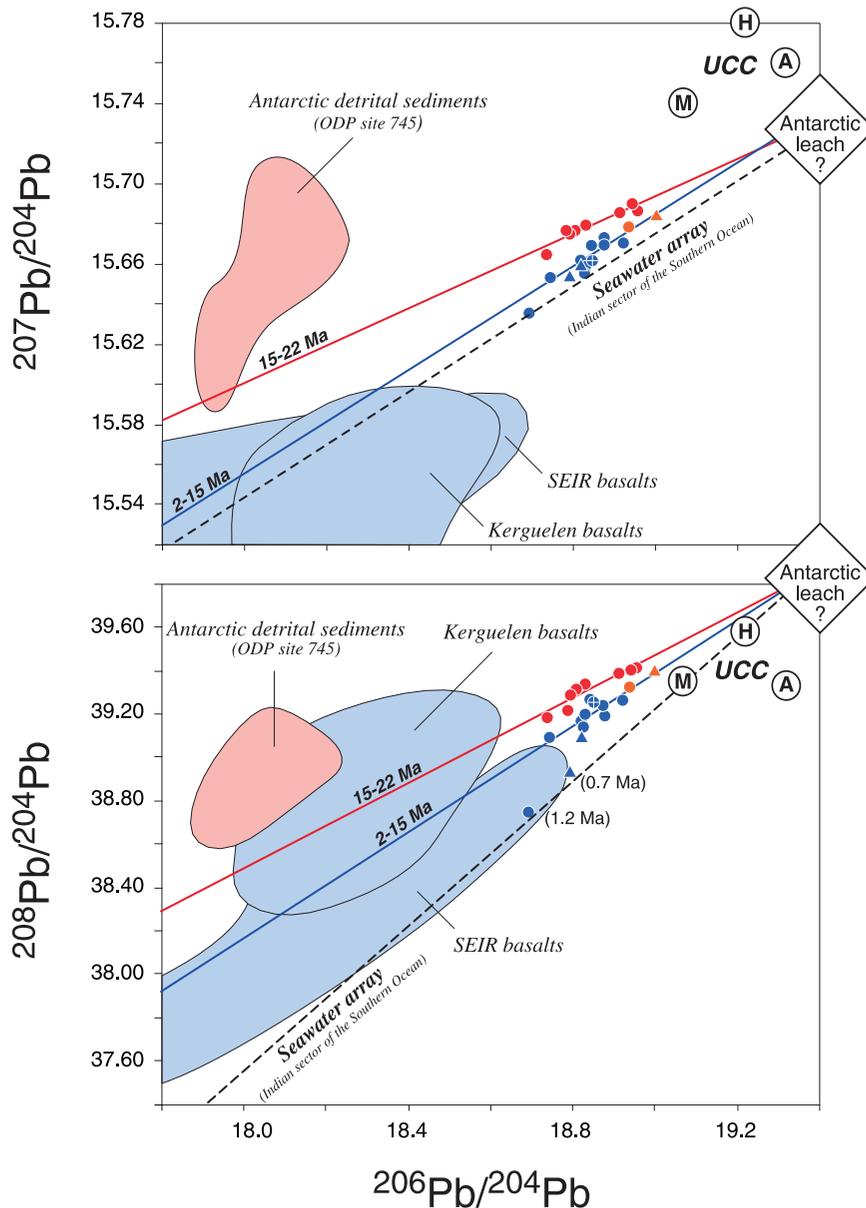
Figure 12. Pb isotopic signatures of site 266 sediments compared to those of potential sources. Isotopic fields are shown for East Antarctic detrital sediments recovered from ODP site 745 [*Joseph et al.*, 2002], basalts from the Kerguelen plateau and the South East Indian Ridge (SEIR) (MPI Georoc database, http://georoc.mpch-mainz.gwdg.de/georoc/), average Upper Continental Crust (UCC) from *Millot et al.* [2004] (M), *Asmerom and Jacobsen* [1993] (A), *Hemming and McLennan* [2001] (H). Antarctic rock data [*DePaolo et al.*, 1982; *Wareham et al.*, 1998; *Hoch et al.*, 2001] are not shown since most of them plot out of the scale of this diagram. The seawater array in the Indian sector of the Southern Ocean is also shown [*Vlastélic et al.*, 2001]. When necessary, literature data have been normalized to the NBS981 values recommended by *Todt et al.* [1996]. Best fit lines are shown for the 2–15 and 15–22 Ma time periods.

explain why dissolved inputs from Antarctica were the highest during the MMCO and decreased afterward. In support of that scenario, ratios of a mobile element over a less mobile element (such as La/Nb) indicate that chemical weathering increased from 22 to ~15 Ma and subsequently decreased (Figure 7). The reduction of chemical weathering after 15 Ma most likely results from East Antarctic ice sheet expansion to continental scale [*Shackleton and Kennett*, 1975].
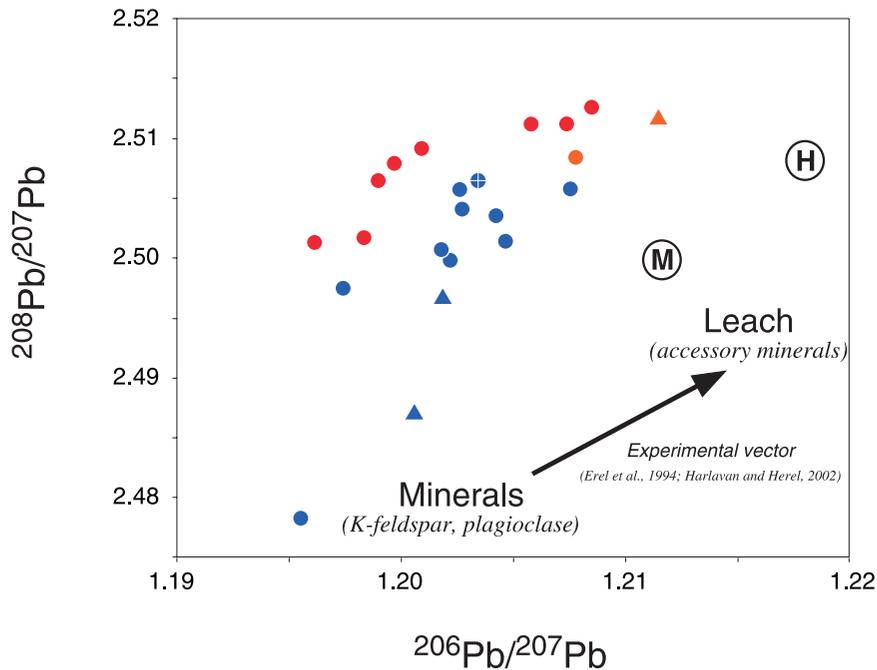
Figure 13. Plot of ^{208}Pb/^{207}Pb versus ^{206}Pb/^{207}Pb. Pb isotopic covariations at site 266 are compared to leaching experiments on granitoids. This figure shows that the isotopic arrays identified at site 266 are subparallel to the experimental vector that links mineral and leach compositions [from *Erel et al.*, 1994; *Harlavan and Erel*, 2002]. This observation raises the possibility that each array results from mixing radiogenic leach and unradiogenic minerals, both derived from the same parental rocks. Averaged compositions of the upper continental crust are indicated (M, *Millot et al.* [2004]; H, *Hemming and McLennan* [2001]).

[20] Such expansion may also have affected the sediment evacuation mode. In an Early Miocene ice-free Antarctica, crustal debris were most likely transported to the ocean by rivers and subsequently distributed by oceanic circulation. *Hayes et al.* [1975] reported in site 266 sediment pile small amounts of coarse sand from the surface down to the carbonate-siliceous transition. This observation may reflect the presence of icebergs in the area since the Middle Miocene. Alternatively, sea level lowering during the Miocene could have enhanced continental slope instability and triggered submarine avalanches. There is, however, no evidence for such catastrophic event at site 266 and the presence of sand most likely results from ice-rafting. As pointed out by *Bareille et al.* [1994], the relative importance of ice-rafting and hydrographic transport modes remains difficult to evaluate. Hf isotopes may place some constraints because Hf-bearing minerals (i.e., Zircons) are normally not transported to the deep sea like clay, but accumulate near the continental shelf [*Patchett et al.*, 1984]. In the absence of evidence for catastrophic sedimentary processes, only icebergs can transport and deliver sands with a continental (unradiogenic) Hf signature to the deep ocean. At

site 266, εHf does not decrease through time, as expected if sediments were increasingly transported by icebergs, but instead increases. This observation indicates that the change in the mode of sediment transport associated with Antarctic glaciation may not have played a major role in the detrital supply to the deep sea.

5.4.2. Hydrographic Processes

[21] *Kolla et al.* [1978] proposed that the distribution of terrigenous sediments in the southeast Indian Ocean is predominantly controlled by hydrographic processes and emphasized the role played by Antarctic Bottom Water (AABW). *Bareille et al.* [1994] interpreted Sr isotope distribution in Quaternary sediments of the area in terms of mixing between Kerguelen and Antarctic detrital inputs. In particular, they observed an eastward decrease of the Kerguelen component, which they attributed to the influence of the ACC. In contrast, Antarctic inputs dominate south of 60°S and may be controlled by the formation of AABW [*Dia et al.*, 1992; *Bareille et al.*, 1994]. The sediments deposited in the southwestern flank of the Australian-Antarctic basin (ODP site 745,

Figure 1) at a similar depth to that of site 266 (4082 m cf 4173 m) show a dominant Antarctic provenance (εNd ∼ −16) since the late Miocene [*Joseph et al.*, 2002], which contrasts with the mixed provenance of the detrital fraction at site 266 during the same period (Figure 14). A likely explanation based on present-day deep circulation pattern (Figure 15) is that site 745 is directly
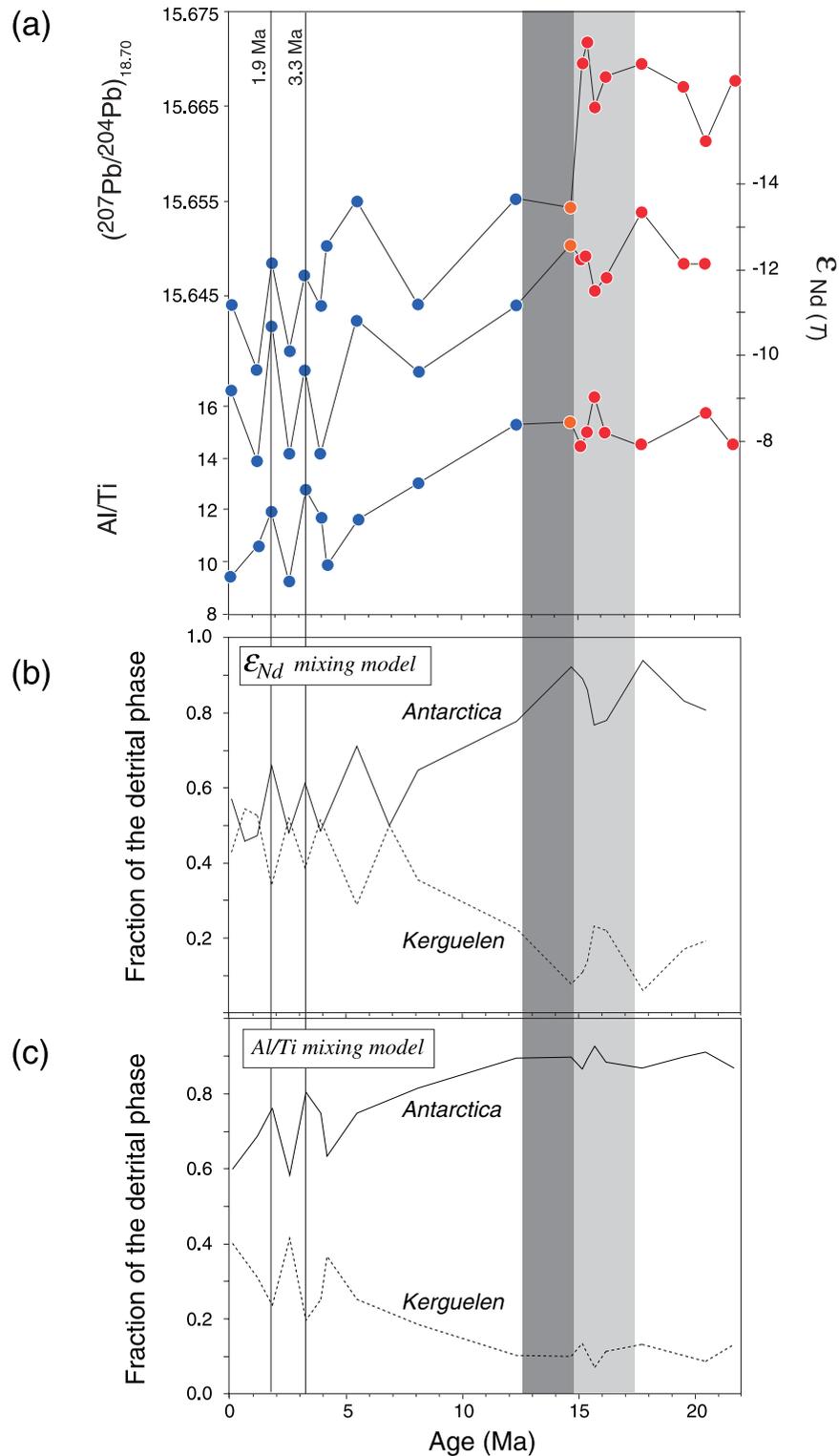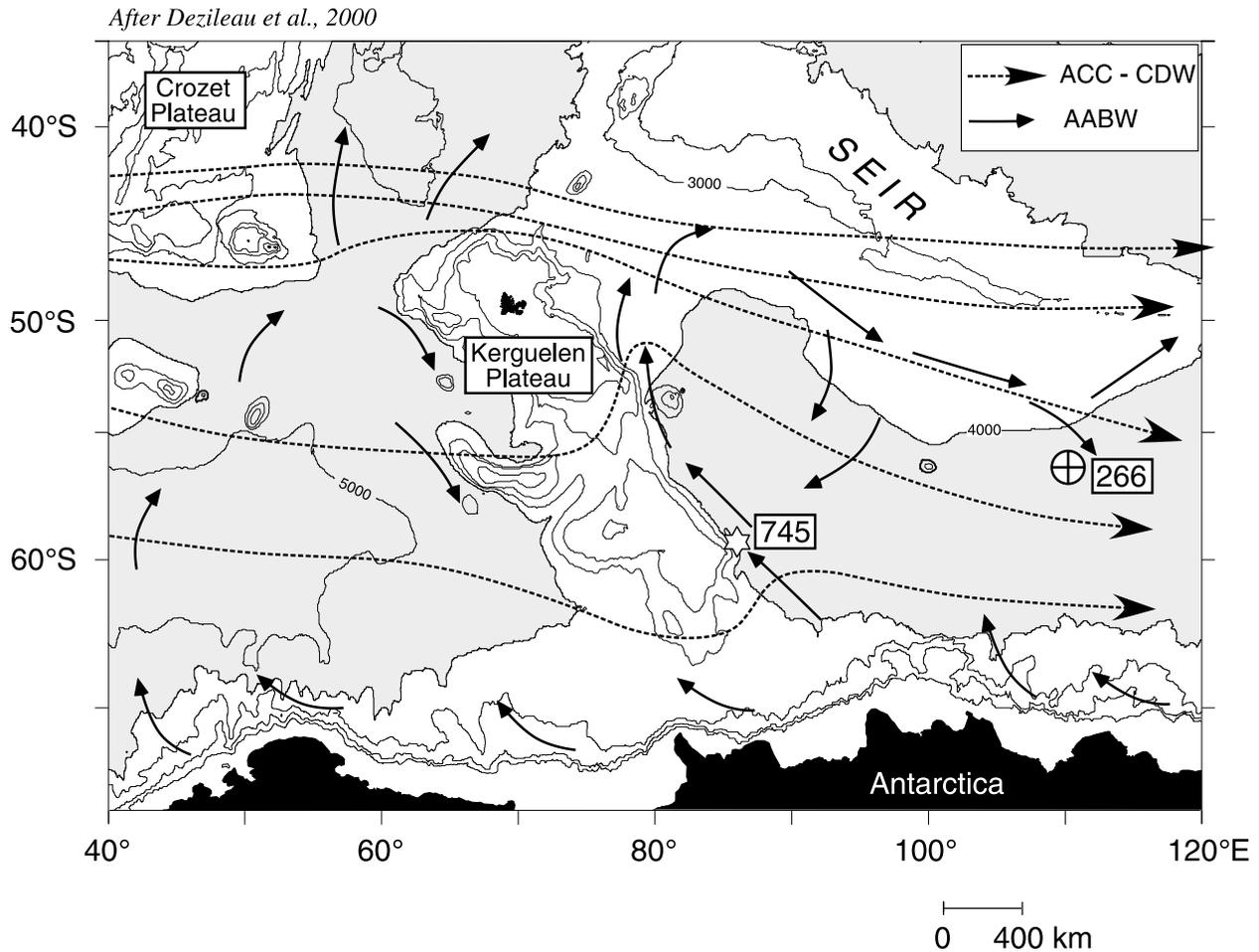

Figure 14

After Dezileau et al., 2000

Figure 15. Circumpolar Deep Water (CDW) and Antarctic Bottom Water (AABW) flows in the Indian sector of the Circum Antarctic Ocean [from *Delizeau et al.*, 2000].

Figure 14. Mixing model. (a) Covariations between $(^{207}Pb/^{204}Pb)_{18.70}$, εNd, and Al/Ti. Samples plotting off major element correlations are not shown. As explained in text, $(^{207}Pb/^{204}Pb)_{18.70}$ is thought to represent the $^{207}Pb/^{204}Pb$ ratio of the detrital fraction. $(^{207}Pb/^{204}Pb)_{18.70}$ is obtained in $^{207}Pb/^{204}Pb$ versus $^{206}Pb/^{204}Pb$ space by projecting each data point to a given value of $^{206}Pb/^{204}Pb$, arbitrarily chosen at 18.70. The projection is made along lines linking each data point ("s") to the intersection of the two main arrays ("c") $((^{206}Pb/^{204}Pb)_c = 19.305, (^{207}Pb/^{204}Pb)_c = 15.716))$. $(^{207}Pb/^{204}Pb)_{18.70}$ is calculated according to $(^{207}Pb/^{204}Pb)_{18.70} = 18.70\ a + b$, with $a = [(^{207}Pb/^{204}Pb)_s - (^{207}Pb/^{204}Pb)_c]/[(^{206}Pb/^{204}Pb)_s - (^{206}Pb/^{204}Pb)_c]$ and $b = (^{207}Pb/^{204}Pb)_s - a(^{206}Pb/^{204}Pb)_c$. The remarkable covariations between $(^{207}Pb/^{204}Pb)_{18.70}$, εNd, and Al/Ti most likely reflect temporal change in the provenance of the detrital fraction. (b) Three-component mixing model based on Nd isotopes. The three end-member components are Antarctic debris (A), Kerguelen debris (K), and seawater fraction (SW). The concentrations and εNd values used are $Nd_A = 26$ ppm, $\varepsilon Nd_A = -18$; $Nd_K = 33$ ppm, $\varepsilon Nd_K = -0.12$ (data from *Joseph et al.* [2002], *McLennan* [2001], and the Georoc database of the MPI). The isotopic composition of seawater in the south Indian Ocean, as recorded by the Fe-Mn crust 109D-C [*O'Nions et al.*, 1998], has varied little since the early Miocene, and a constant value of -7.8 is used in the model. Seawater-derived Nd is inferred from $Nd_{SW} = Nd_{bulk} - (Al_2O_{3\ sample} \cdot [Nd/Al_2O_3]_{det})$, where $[Al_2O_3]_{det} = 15.2$ wt.% and $[Nd]_{det} = 29$ ppm. The fractions of Antarctic and Kerguelen material, identified as x_A and x_K, respectively, are obtained by solving the following equation: $x_K.Nd_K.(\varepsilon Nd_{Sample} - \varepsilon Nd_K) + x_A.Nd_A.(\varepsilon Nd_{Sample} - \varepsilon Nd_A) + Nd_{SW}.(\varepsilon Nd_{Sample} - \varepsilon Nd_{SW}) = 0$, with $x_A + x_K = 1$. (c) Two-component mixing model based on Al/Ti. The two end-member components are Antarctic debris (A) and Kerguelen debris (K). Seawater-derived Al and Ti are neglected here. End-member compositions used are (in wt.%) $Al_K = 8.02$, $Ti_K = 1.52$, $Al_A = 8.04$, $Ti_K = 0.41$ (data from *McLennan* [2001] and the Georoc database of the MPI). x_A and x_K are obtained by solving the following equation: $x_K.[Ti_K.(Al/Ti)_{sample} - Al_K] + x_A.[Ti_A.(Al/Ti)_{sample} - Al_A] = 0$ with $x_A + x_K = 1$.

influenced by deep water formed near the Antarctic margin (AABW), whereas site 266 sees more a mixture of AABW and Circumpolar Deep water (CDW). Because CDW flows eastward over the Kerguelen plateau, mostly north of 55°S, it may deliver Kerguelen volcanic debris to the north Australian-Antarctica basin [*Dezileau et al.*, 2000]. These observations suggest that hydrographic processes, and, in particular, the relative influence of AABW and CDW, control sediment provenance within the Australian-Antarctic basin. Moreover, trace elements and Sr isotope variations during the last climatic cycles indicate that detrital input from the Kerguelen plateau increased during glacial periods, most likely reflecting an enhanced CDW influence [*Dezileau et al.*, 2000; *Bareille et al.*, 1994]. In the Atlantic sector of the Southern Ocean, increased detrital input from southern sources during glacial periods may have resulted from an increased influence of CDW as well [*Bayon et al.*, 2003]. However, from these Quaternary studies, it is not clear whether the inferred increased influence of CDW during glacial periods reflects an increased flow of CDW or increased concentration of suspended material. *Bareille et al.* [1994] argued that sea level lowering during glacial periods could enhance instability and erosion of the newly emerged terrains, resulting in a more efficient detrital input to the ocean. According to *Dezileau et al.* [2000], the marked increase of the erosion of the Kerguelen-Crozet volcanic plateau during the last glacial period is consistent with strengthening of the ACC. Our long-term geochemical study suggests that the Miocene transition toward cold climate may also have enhanced the influence of CDW. Because there is no obvious reason why sea level lowering during the Miocene would have led to a preferential erosion of the Kerguelen plateau, it is suggested that the inferred enhanced influence of CDW reflects strengthening of the ACC.

[22] Although early and middle Miocene deepwater circulation patterns are still debated [*Wright et al.*, 1992], there is a general consensus regarding two main features: (1) NADW initiated during the Middle Miocene [*Schnitker*, 1980; *Blanc et al.*, 1980; *Woodruff and Savin*, 1989]. (2) A Northern deep water source (Tethyan Indian Saline Water) ventilated the deep Indian basin in the Early Miocene and was progressively replaced during the middle Miocene by a southern component (AABW) as Tethyan seaway closed and East Antarctic ice sheet developed [*Woodruff and Savin*,

1989; *Wright et al.*, 1992; *Flower and Kennett*, 1995]. The isotopic record from site 266 indicates that the initiation of AABW did not increase Antarctic detrital input to the Southern Ocean, which rather diminished as a result of Antarctic glaciation. Our data raise the possibility that the ACC initiated during the Miocene, in which case NADW production and ACC would have initiated at the same period. In addition, isotopes and Al/Ti suggest that ACC reached it present-day strength between 4 and 7 Ma ago. Isotopes and Al/Ti spikes at 1.9 and 3.3 Ma may reflect a reduction in ACC strength. Alternatively, they may reflect temporary enhanced inputs from Antarctica resulting from East Antarctic ice sheet instability [*Joseph et al.*, 2002].

6. Conclusions

[23] The geochemical study of DSDP site 266 led to the following conclusions:

[24] 1. Pb, Nd and Hf isotopes as well as Al/Ti ratios indicate a change of sediment provenance during the Middle Miocene climate transition. This change could correspond to a reduction of Antarctic input, an increase of Kerguelen input, or both.

[25] 2. Mixing models based on Nd isotopes and Al/Ti suggest a 30–40% reduction of Antarctic input and an equivalent increase of Kerguelen input during the Miocene. Reduction of the Antarctic input may result from the formation of a stable East Antarctic ice sheet, whereas increase of Kerguelen input may reflect the initiation, or enhancement of the Antarctic Circumpolar Current.

[26] 3. Pb isotopic variations are complex since they record the effects of two processes: a change of sediment provenance and the type and intensity of weathering and erosion. Considering that the products of chemical weathering of Antarctic granite dominantly control the $^{206}Pb/^{204}Pb$ signature of bulk sediment, constraints can be placed on erosion processes. In agreement with trace element systematics, Pb isotopes suggest that chemical weathering was at its maximum during the Middle Miocene climatic optimum and decreased afterward.

[27] 4. Because Hf resides in dense resistant minerals (zircons) that are possibly transported by icebergs, but not by turbidity currents, Hf isotopes may be used to evaluate the sediment transport mode (hydrographic versus ice-rafted). Although small amounts of ice-rafted material have been previously identified in the upper unit [*Hayes et*

al., 1975], Hf isotopes do not indicate that icebergs became a dominant mode of sediment transport during the Miocene.

[28] 5. Large geochemical oscillations occurred during the Pliocene, possibly reflecting fluctuation in the strength of the Antarctic Circumpolar Current or, alternatively, periods of instability of the East Antarctic ice sheet.

Acknowledgments

References

Abouchami, W., and S. Goldstein (1995), A lead isotopic study of Circum-Antarctic manganese nodules, *Geochim. Cosmochim. Acta*, *59*, 1809–1820.

Abouchami, W., and M. Zabel (2003), Climate forcing of the Pb isotope record of terrigenous input into the Equatorial Atlantic, *Earth Planet. Sci. Lett.*, *213*, 221–234.

Albarède, F., S. L. Goldstein, and D. Dautel (1997), The neodymium isotopic composition of manganese nodules from the Southern and Indian oceans, the global oceanic neodymium budget, and their bearing on deep ocean circulation, *Geochim. Cosmochim. Acta*, *61*, 1277–1291.

Albarède, F., A. Simonetti, J. D. Vervoort, J. Blichert-Toft, and W. Abouchami (1998), A Hf-Nd isotopic correlation in ferromanganese nodules, *Geophys. Res. Lett.*, *25*, 3895–3898.

Allègre, C.-J., B. Dupré, and E. Lewin (1986), Thorium/uranium ratio of the Earth, *Chem. Geol.*, *56*, 219–227.

Asmerom, Y., and S. B. Jacobsen (1993), The Pb isotopic evolution of the Earth: Inferences from river water suspended loads, *Earth Planet. Sci. Lett.*, *115*, 245–256.

Bareille, G., F. E. Grousset, M. Labracherie, L. D. Labeyrie, and J.-R. Petit (1994), Origin of detrital fluxes in the southeast Indian Ocean during the last climatic cycle, *Paleoceanography*, *9*, 799–819.

Bayon, G., C. R. German, R. M. Boella, J. A. Milton, R. N. Taylor, and R. W. Nesbitt (2002), An improved method for extracting marine sediment fractions and its application to Sr and Nd isotopic analysis, *Chem. Geol.*, *187*, 179–199.

Bayon, G., C. R. German, R. W. Nesbitt, P. Bertrand, and R. R. Schneider (2003), Increased input of circumpolar deep water-borne detritus to the glacial SE Atlantic Ocean, *Geochem. Geophys. Geosyst.*, *4*(3), 1025, doi:10.1029/2002GC000371.

Blanc, P.-L., D. Rabussier, C. Vergnaud-Grazzini, and J.-C. Duplessy (1980), North Atlantic Deep Water formed by the later middle Miocene, *Nature*, *283*, 553–555.

Blichert-Toft, J., C. Chauvel, and F. Albarède (1997), Separation of Hf and Lu for high-precision isotope analysis of rock samples by magnetic sector-multiple collector ICP-MS, *Contrib. Mineral. Petrol.*, *127*, 248–260.

DePaolo, D. J., W. I. Manton, E. S. Grew, and M. Halpern (1982), Sm-Nd, Rb-Sr and U-Th-Pb systematics of granulite facies rocks from Fyfe Hills, Enderby Land, Antarctica, *Nature*, *298*, 614–618.

Dezileau, L., G. Bareille, J. L. Reyss, and F. Lemoine (2000), Evidence for strong sediment redistribution by bottom currents along the southeast Indian ridge, *Deep Sea Res., Part I*, *47*, 1899–1936.

Dia, A., B. Dupré, and C. J. Allègre (1992), Nd isotopes in Indian Ocean sediments used as a tracer of supply to the ocean and circulation paths, *Mar. Geol.*, *103*, 349–359.

Eggins, S. M., J. D. Woodhead, L. P. J. Kinsley, G. E. Mortimer, P. Sylvester, M. T. McCulloch, J. M. Hergt, and M. R. Handler (1997), A simple method for the precise determination of ≥40 trace elements in geological samples by ICPMS using enriched isotope internal standardization, *Chem. Geol.*, *134*, 311–326.

Ehrmann, W. U., and A. Mackensen (1992), Sedimentological evidence for the formation of an East Antarctic ice sheet in Eocene/Oligocene time, *Palaeogeogr. Palaeoclimatol. Palaeoecol.*, *93*, 85–112.

Erel, Y., Y. Harlavan, and J. D. Blum (1994), Lead isotope systematics of granitoid weathering, *Geochim. Cosmochim. Acta*, *58*, 5299–5306.

Exon, N., et al. (2002), Drilling reveals climatic consequences of Tasmanian gateway opening, *Eos Trans. AGU*, *83*(23), 253, 258–259.

Flower, B. P., and J. P. Kennett (1993), Middle Miocene ocean-climate transition: High-resolution oxygen and carbon isotopic records from Deep Sea Drilling project Site 588A, southwest Pacific, *Paleoceanography*, *8*, 811–843.

Flower, B. P., and J. P. Kennett (1995), Middle Miocene deep-water paleoceanography in the southwest Pacific: Relation with East Antarctic ice sheet development, *J. Geophys. Res.*, *10*, 1095–1112.

Frank, M., N. Whiteley, S. Kasten, J. R. Hein, and K. O'Nions (2002), North Atlantic Deep Water export to the Southern Ocean over the past 14 Myr: Evidence from Nd and Pb isotopes in ferromanganese crusts, *Paleoceanography*, *17*(2), 1022, doi:10.1029/2000PA000606.

Hallet, B., L. Hunter, and J. Bogen (1996), Rates of erosion and sediment evacuation by glaciers: A review of field data and their implications, *Global Planet. Change*, *12*, 213–235.

Harlavan, Y., and Y. Erel (2002), The release of Pb and REE from granitoids by the dissolution of accessory phases, *Geochim. Cosmochim. Acta*, *66*, 837–848.

Harlavan, Y., Y. Erel, and J. D. Blum (1998), Systematic changes in lead isotopic composition with soil age in glacial granitic terrains, *Geochim. Cosmochim. Acta*, *62*, 33–46.

Hayes, D. E., et al. (1975), *Initial Reports of the Deep Sea Drilling Project*, vol. 28, pp. 81–119, U.S. Govt. Print. Off., Washington, D. C.

Hemming, S. R., and S. M. McLennan (2001), Pb isotopic composition of modern deep sea turbidites, *Earth Planet. Sci. Lett.*, *184*, 489–503.

Hoch, M., M. Rehkämper, and H. J. Tobschall (2001), Sr, Nd, Pb and O isotopes of minettes from Schirmacher Oasis, East Antarctica: A case of mantle metasomatism involving subducted continental material, *J. Petrol.*, *42*, 1387–1400.

Hofmann, A. W. (1988), Chemical differentiation of the Earth: The relationship between mantle, continental crust, and oceanic crust, *Earth Planet. Sci. Lett.*, *90*, 297–314.

Joseph, L. H., D. K. Rea, B. A. van der Pluijm, and J. D. Gleason (2002), Antarctic environmental variability since the late Miocene: ODP Site 745, The East Kerguelen sediment drift, *Earth Planet. Sci. Lett.*, *201*, 127–142.

Keller, G., and J. A. Barron (1983), Paleoceanographic implications of Miocene deep-sea hiatuses, *Geol. Soc. Am. Bull.*, *94*, 590–613.

Kennett, J. P. (1977), Cenozoic evolution of Antarctic glaciation, the circum-Antarctic ocean and their impact on global paleoceanography, *J. Geophys. Res.*, *82*, 3843–3859.

Kolla, V., L. Henderson, L. Sullivan, and P. E. Biscaye (1978), Recent sedimentation in the southeast Indian Ocean with special reference to the effects of Antarctic bottom water circulation, *Mar. Geol.*, *27*, 1–17.

Lugmair, G. W., and S. J. G. Galer (1992), Age and isotopic relationships among the angrites Lewis Cliff 86010 and Angra dos Reis, *Geochim. Cosmochim. Acta*, *56*, 1673–1694.

Matthews, R. K., and R. Z. Poore (1980), Tertiary $\delta^{18}O$ record and glacio-eustatic sea-level fluctuations, *Geology*, *8*, 501–504.

McLennan, S. M. (2001), Relationships between the trace element composition of sedimentary rocks and upper continental crust, *Geochem. Geophys. Geosyst.*, *2*(4), doi:10.1029/2000GC000109.

Miller, K. G., R. G. Fairbanks, and G. S. Mountain (1987), Tertiary oxygen isotope synthesis, sea level history, and continental margin erosion, *Paleoceanography*, *2*, 1–19.

Miller, K. G., J. D. Wright, and R. G. Fairbanks (1991), Unlocking the icehouse: Oligocene-Miocene oxygen isotope, eustasy, and margin erosion, *J. Geophys. Res.*, *96*, 6829–6848.

Millot, R., C.-J. Allègre, J. Gaillardet, and S. Roy (2004), Lead isotopic systematics of major river sediments: A new estimate of the Pb isotopic composition of the upper continental crust, *Chem. Geol.*, *203*, 75–90.

Murray, R. W., and M. Leinen (1993), Chemical transport to the seafloor of the equatorial Pacific Ocean across a latitudinal transect at 135°W: Tracking sedimentary major, trace and rare earth element fluxes at the Equator and the Intertropical Convergence Zone, *Geochim. Cosmochim. Acta*, *57*, 4141–4163.

O'Nions, R. K., M. Frank, F. von Blanckenburg, and H.-F. Ling (1998), Secular variation of Nd and Pb isotopes in ferromanganese crusts from the Atlantic, Indian and Pacific Oceans, *Earth Planet. Sci. Lett.*, *155*, 15–28.

Patchett, P. J., W. M. White, H. Feldmann, S. Kielinczuk, and A. W. Hofmann (1984), Hafnium/rare earth element fractionation in the sedimentary system and crustal recycling into the Earth's mantle, *Earth Planet. Sci. Lett.*, *69*, 365–378.

Piotrowski, A. M., D.-C. Lee, J. N. Christensen, K. W. Burton, A. N. Halliday, J. R. Hein, and D. Günther (2000), Changes in erosion and ocean circulation recorded in the Hf isotopic compositions of North Atlantic and Indian Ocean ferromanganese crusts, *Earth Planet. Sci. Lett.*, *181*, 315–325.

Piotrowski, A. M., S. L. Goldstein, S. R. Hemming, and R. G. Fairbanks (2004), Intensification and variability of ocean thermohaline circulation through the last deglaciation, *Earth Planet. Sci. Lett.*, *225*, 205–220.

Piper, D. Z. (1974), Rare earth elements in the sedimentary cycle: A summary, *Chem. Geol.*, *14*, 285–304.

Rutberg, R. L., S. R. Hemming, and S. L. Goldstein (2000), Reduced North Atlantic Deep Water flux to the glacial Southern Ocean inferred from neodymium isotope ratios, *Nature*, *405*, 935–938.

Schnitker, D. (1980), North Atlantic oceanography as possible cause of Antarctic glaciation and eutrophication, *Nature*, *284*, 615–616.

Shackleton, N. J., and J. P. Kennett (1975), Paleotemperature history of the Cenozoic and the initiation of Antarctic glaciation: Oxygen and carbon analysis in DSDP sites 277, 279 and 281, *Initial Rep. Deep Sea Drill. Proj.*, *29*, 743–755.

Todt, W., R. A. Cliff, A. Hanser, and A. W. Hofmann (1996), Evaluation of a ^{202}Pb-^{205}Pb double spike for high-precision lead isotope analysis, in *Earth Processes: Reading the Isotopic Code*, Geophys. Monogr. Ser., vol. 95, edited by A. Basu and S. Hart, pp. 429–437, AGU, Washington, D. C.

Vervoort, J. D., P. J. Patchett, J. Blichert-Toft, and F. Albarède (1999), Relationships between Lu-Hf and Sm-Nd isotopic systems in the global sedimentary system, *Earth Planet. Sci. Lett.*, *168*, 79–99.

Vlastélic, I., W. Abouchami, S. J. G. Galer, and A. W. Hofmann (2001), Geographic control on Pb isotope distribution and sources in Indian Ocean Fe-Mn deposits, *Geochim. Cosmochim. Acta*, *65*, 4303–4319.

von Blanckenburg, F., and T. F. Nägler (2001), Weathering versus circulation-controlled changes in radiogenic isotope tracer composition of the Labrador Sea and North Atlantic Deep Water, *Paleoceanography*, *16*, 424–434.

Walder, A. J., and N. Furuta (1993), High precision lead isotope ratio measurement by inductively coupled plasma multiple collector mass spectrometry, *Anal. Sci.*, *9*, 675–680.

Walter, H. J., E. Hegner, B. Diekmann, G. Kuhn, and M. M. Rutgers van der Loeff (2000), Provenance and transport of terrigenous sediment in the South Atlantic Ocean and their relations to glacial and interglacial cycles: Nd and Sr isotopic evidence, *Geochim. Cosmochim. Acta*, *64*, 3813–3827.

Wareham, C. D., R. J. Pankhurst, R. J. Thomas, B. C. Storey, G. H. Grantham, J. Jacobs, and B. M. Eglington (1998), Pb, Nd and Sr isotope mapping of Grenville-age crustal provinces in Rodinia, *J. Geol.*, *106*, 647–659.

White, W. M., F. Albarède, and P. Télouk (2000), High-precision analysis of Pb isotope ratios by multi-collector ICP-MS, *Chem. Geol.*, *167*, 257–270.

Woodruff, F., and S. M. Savin (1989), Miocene deepwater oceanography, *Paleoceanography*, *4*, 87–140.

Woodruff, F., and S. M. Savin (1991), Mid-Miocene isotope stratigraphy in the deep sea: High-resolution correlations, paleoclimatic cycles, and sediment preservation, *Paleoceanography*, *6*, 755–806.

Wright, J. D., and K. G. Miller (1992), Miocene stable isotope stratigraphy, Site 747, Kerguelen Plateau, *Proc. Ocean Drilling Prog., Sci. Results*, *120*, 855–866.

Wright, J. D., K. G. Miller, and R. G. Fairbanks (1992), Early and middle Miocene stable isotopes: Implications for deepwater circulation and climate, *Paleoceanography*, *7*, 357–389.

Zachos, J., M. Pagani, L. Sloan, E. Thomas, and K. Billups (2001), Trends, rhythms, and aberrations in global climate 65 Ma to present, *Science*, *27*, 686–693.